

# The escape of heavy atoms from the ionosphere of HD209458b. II. Interpretation of the observations

T. T. Koskinen<sup>a,\*</sup>, R. V. Yelle<sup>a</sup>, M. J. Harris<sup>b</sup>, P. Lavvas<sup>c</sup>

<sup>a</sup>*Lunar and Planetary Laboratory, University of Arizona, 1629 E. University Blvd., Tucson, AZ 85721, USA*

<sup>b</sup>*Department of Physics and Astronomy, University College London, Gower Street, London WC1E 6BT, UK*

<sup>c</sup>*Groupe de Spectrométrie Moléculaire et Atmosphérique UMR CNRS 6089, Université Reims Champagne-Ardenne, 51687, France*

---

## Abstract

Transits in the H I 1216 Å (Lyman α), O I 1334 Å, C II 1335 Å, and Si III 1206.5 Å lines constrain the properties of the upper atmosphere of HD209458b. In addition to probing the temperature and density profiles in the thermosphere, they have implications for the properties of the lower atmosphere. Fits to the observations with a simple empirical model and a direct comparison with a more complex hydrodynamic model constrain the mean temperature and ionization state of the atmosphere, and imply that the optical depth of the extended thermosphere of the planet in the atomic resonance lines is significant. In particular, it is sufficient to explain the observed transit depths in the H I 1216 Å line. The detection of O at high altitudes implies that the minimum mass loss rate from the planet is approximately  $6 \times 10^6 \text{ kg s}^{-1}$ . The mass loss rate based on our hydrodynamic

---

\*Corresponding author. Fax: +1 (520) 621 4933  
*Email address:* tommy@lpl.arizona.edu (T. T. Koskinen)

model is higher than this and implies that diffusive separation is prevented for neutral species with a mass lower than about 130 amu by the escape of H. Heavy ions are transported to the upper atmosphere by Coulomb collisions with  $\text{H}^+$  and their presence does not provide as strong constraints on the mass loss rate as the detection of heavy neutral atoms. Models of the upper atmosphere with solar composition and heating based on the average solar X-ray and EUV flux agree broadly with the observations but tend to underestimate the transit depths in the O I, C II, and Si III lines. This suggests that the temperature and/or elemental abundances in the thermosphere may be higher than expected from such models. Observations of the escaping atmosphere can potentially be used to constrain the strength of the planetary magnetic field. We find that a magnetic moment of  $m \lesssim 0.04 m_J$ , where  $m_J$  is the Jovian magnetic moment, allows the ions to escape globally rather than only along open field lines. The detection of  $\text{Si}^{2+}$  in the thermosphere indicates that clouds of forsterite and enstatite do not form in the lower atmosphere. This has implications for the temperature and dynamics of the atmosphere that also affect the interpretation of transit and secondary eclipse observations in the visible and infrared wavelengths.

*Keywords:* Extra-solar planets, Aeronomy, Atmospheres, composition, Photochemistry

---

## 1. Introduction

The detection of H, O, C<sup>+</sup>, and Si<sup>2+</sup> in the upper atmosphere of HD209458b (Vidal-Madjar et al., 2003, 2004; Linsky et al., 2010), and the tentative detection of H in the upper atmosphere of HD189733b (Lecavelier des Etangs et al., 2010) and Mg<sup>+</sup> in the upper atmosphere of WASP-12b (Fossati et al., 2010) are among the most exciting recent discoveries related to the atmospheres of extrasolar giant planets (EGPs). The observations demonstrate that the the upper atmospheres of close-in EGPs such as HD209458b differ significantly from the thermospheres of the giant planets in the solar system.

They are much hotter, they extend to several planetary radii and instead of molecular hydrogen, they are primarily composed of atoms and atomic ions.

The detection of heavy atoms and ions such as O, C<sup>+</sup>, Si<sup>2+</sup>, and Mg<sup>+</sup> implies that the atmospheres of close-in EGPs are not always affected by diffusive separation. A likely explanation is that diffusive separation of the heavy atoms and ions is prevented by momentum transfer collisions with the rapidly escaping light atoms and ions. Mass fractionation during hydrodynamic escape is believed to have played an important role in the early evolution of the atmospheres of the terrestrial planets (e.g., Zahnle and Kasting, 1986; Hunten et al., 1987) but it cannot be observed in action anywhere in the solar system. Observations of EGP atmospheres thus provide a unique opportunity to study this phenomenon that should lead to a better understanding of evolutionary processes in our own solar system.

Extended thermospheres give rise to large transit depths in UV trans-

mission spectra. However, they are also potentially detectable in optical and infrared spectra. For instance, Coustenis et al. (1997, 1998) searched for an exosphere around 51 Peg b in the near-IR. In line with the current understanding, they suggested that the exospheres of close-in EGPs such as 51 Peg b are hot and composed primarily of atoms and ions. They also argued that hydrodynamic escape can lead to the escape of heavier species, and give rise to large in-transit absorption by such species in optical and near-IR spectra. However, 51 Peg b is not a transiting planet and the search for an exosphere around it was not successful. On the other hand, once the transit of HD209458b was first detected (Charbonneau et al., 2000; Henry et al., 2000), similar searches on this planet were also undertaken.

Moutou et al. (2001) looked for visible absorption by species such as Na, H, He,  $\text{CH}^+$ ,  $\text{CO}^+$ ,  $\text{N}_2^+$ , and  $\text{H}_2\text{O}^+$  in the upper atmosphere of HD209458b. These observations were followed by Moutou et al. (2003) who attempted to measure the transit depth in the He 1083 nm line that was predicted to be significant by Seager and Sasselov (2000). The most recent searches were reported by Winn et al. (2004) and Narita et al. (2005) who looked for transits in the visible Na D, Li,  $\text{H}\alpha$ ,  $\text{H}\beta$ ,  $\text{H}\gamma$ , Fe, and Ca absorption lines. So far none of the ground-based searches have led to a detection of the upper atmosphere. However, the non-detection is based on only a few observations that have proven difficult to analyze, and the search should continue.

Visible and infrared observations have been able to probe the atmosphere of HD209458b at lower altitudes. In fact, HD209458b was the first EGP

47 to have its atmosphere detected by transmission spectroscopy. The first  
 48 detection was achieved by Charbonneau et al. (2002) who observed a deeper  
 49 in-transit absorption in the Na D 589.3 nm resonance doublet compared to  
 50 the adjacent wavelength bands. This detection was based on four transits  
 51 observed with the Space Telescope Imaging Spectrograph (STIS) onboard the  
 52 Hubble Space Telescope (HST) (Brown et al., 2001). The same data were  
 53 later reanalyzed by Sing et al. (2008a,b) who combined them with other  
 54 observations (Knutson et al., 2007) and created a transmission spectrum of  
 55 HD209458b at wavelengths of 300–800 nm. They argued that the abundance  
 56 of sodium in the atmosphere is depleted above the 3 mbar level either by  
 57 condensation into Na<sub>2</sub>S clouds or ionization. We note that the detection of  
 58 Si<sup>2+</sup> in the thermosphere (Linsky et al., 2010) constrains cloud formation  
 59 mechanisms in the upper atmosphere and implies that the depletion of Na  
 60 at low pressures is probably due to ionization (see Section 3.3).

61 The atmosphere of HD209458b has also been observed several times in  
 62 the infrared with the Spitzer space telescope. Deming et al. (2005) detected  
 63 the secondary eclipse of the planet at 24  $\mu$ m by using the Multiband Imaging  
 64 Photometer (MIPS). Together with similar observations of TrES-1 at 4.5 and  
 65 8.0  $\mu$ m obtained by Charbonneau et al. (2005) who used the Infrared Array  
 66 Camera (IRAC), these observations constitute the first detections of infrared  
 67 emission from extrasolar planets. They were followed by Richardson et al.  
 68 (2007) who observed the infrared emission spectrum of HD209458b between  
 69 7.5 and 13.2  $\mu$ m with the Infrared Spectrograph (IRS). This spectrum was

70 reanalyzed by Swain et al. (2008) who noted that it is largely featureless with  
71 some evidence for an unidentified spectral feature between 7.5 and 8.5  $\mu\text{m}$ .

72 Knutson et al. (2008) used IRAC to observe the secondary eclipse of  
73 HD209458b in the 3.6, 4.5, 5.8, and 8.0  $\mu\text{m}$  bands. They observed a higher  
74 than expected flux in the 4.5 and 5.8  $\mu\text{m}$  bands and interpreted this as ev-  
75 idence for the presence of a stratospheric temperature inversion that gives  
76 rise to strong water emission at these wavelengths. Beaulieu et al. (2010)  
77 observed the transit of the planet in the same wavelength bands and also  
78 found evidence for the presence of water vapor in the atmosphere. The de-  
79 tection of water vapor is also supported by Swain et al. (2009) who used the  
80 Near Infrared Camera and Multi-Object Spectrometer (NICMOS) on HST  
81 to observe the secondary eclipse of HD209458b between 1.5 and 2.5  $\mu\text{m}$ . In  
82 addition to water vapor, the NICMOS observations revealed the presence  
83 of methane and carbon dioxide in the emission spectrum. These detections  
84 provide valuable clues to the overall composition of the atmosphere but the  
85 uncertainties in the data and degeneracies between temperature and abun-  
86 dances in the forward model prevent a more quantitative characterization of  
87 the density and temperature profiles.

88 In general, difficulties associated with reducing the data and the need  
89 to describe a few uncertain data points with models of growing complexity  
90 has led to disagreements on the analysis and interpretation of transmission  
91 and secondary eclipse data on different exoplanets. The same is true of the  
92 FUV transit observations of HD209458b. Vidal-Madjar et al. (2003) used the

93 STIS G140M medium resolution grating to detect a  $15 \pm 4$  % transit depth  
 94 in the wings of the stellar H Lyman  $\alpha$  emission line<sup>1</sup>. Based on the data, they  
 95 argued that the planet is followed by a cometary tail of escaping hydrogen  
 96 atoms that are accelerated to velocities in excess of  $100 \text{ km s}^{-1}$  by stellar  
 97 radiation pressure (see also Schneider et al., 1998). Later, Vidal-Madjar et  
 98 al. (2004) used the STIS G140L low resolution grating to detect absorption  
 99 by H, O and C<sup>+</sup> in the upper atmosphere, and argued that the atmosphere of  
 100 HD209458b escapes hydrodynamically. Linsky et al. (2010) used the Cosmic  
 101 Origins Spectrograph (COS) on HST to confirm the detection of C<sup>+</sup> and  
 102 reported on the detection of Si<sup>2+</sup> around the planet. They also argued that  
 103 the atmosphere escapes hydrodynamically.

104 Ben-Jaffel (2007, 2008) disagreed with the interpretation of the G140M  
 105 observations. He reanalyzed the G140M data and argued that the 15 %  
 106 H Lyman  $\alpha$  transit depth was exaggerated because the data were partly  
 107 corrupted by short-term variability of the host star and geocoronal Lyman  $\alpha$   
 108 emissions. He also showed that there is no evidence for a cometary tail in the  
 109 data, and that absorption by H in the extended thermosphere of the planet  
 110 can explain the observations. Ben-Jaffel and Hosseini (2010) reanalyzed the  
 111 G140L data and reached a similar conclusion regarding H (see also Koskinen  
 112 et al., 2010a). However, Ben-Jaffel and Hosseini (2010) fitted the H Lyman  $\alpha$   
 113 observations by scaling the density profiles from the model of Garcia Munoz

---

<sup>1</sup>The core of the H Lyman  $\alpha$  line is entirely absorbed by the interstellar medium (ISM)

114 (2007), and argued that suprathermal O and C<sup>+</sup> are required to fit the transit  
115 depths in the O I and C II lines. They did not explain how the suprathermal  
116 atoms form and simply chose their properties to fit the observations.

117 Holström et al. (2008) offered yet another explanation for the H Lyman  $\alpha$   
118 observations. They argued that hydrogen atoms cannot be sufficiently accel-  
119 erated by stellar radiation pressure before they are ionized by stellar X-rays  
120 and EUV (XUV) radiation. Instead, they suggested that the observed ab-  
121 sorption arises from a cloud of energetic neutral atoms (ENAs) that form by  
122 charge exchange between the protons in the stellar wind and the escaping  
123 hydrogen. In their model, the observed absorption reflects the velocity of  
124 the stellar wind, and the data can potentially be used to characterize the  
125 magnetosphere of the planet. Ekenbäck et al. (2010) recently updated the  
126 model to include a more realistic description of the escaping atmosphere and  
127 stellar wind properties. However, both studies ignored absorption by H in  
128 the thermosphere, which is significant, and did not attempt to explain the  
129 presence of heavier atoms and ions such as O, C<sup>+</sup>, and Si<sup>2+</sup> in the escaping  
130 atmosphere.

131 All of the interpretations of the UV transit data require that HD209458b  
132 has a hot and extended thermosphere. In fact, Koskinen et al. (2010a) (here-  
133 after K10) also showed that absorption by thermal H and O in such a ther-  
134 mosphere explains both the H Lyman  $\alpha$  and O I 1304 Å transit depths.  
135 Further, their model related the observations to a few physically motivated  
136 characteristics such as the mean temperature and composition of the upper



137 atmosphere. They also used the observations to constrain the pressure level  
138 where  $\text{H}_2$  dissociates and estimated that the  $\text{H}_2/\text{H}$  transition should occur  
139 at  $0.1\text{--}1\ \mu\text{bar}$ . However, these results are based on an empirical model that  
140 was simply designed to fit the observations. One of the aims of the current  
141 paper is to show that the results are also supported by more complex physical  
142 models.

143 We have also attempted to establish a more comprehensive description  
144 of the thermosphere that treats it as an integral part of the whole atmo-  
145 sphere rather than a separate entity. In order to do so, we developed a new  
146 one-dimensional escape model for the upper atmosphere of HD209458b that  
147 includes the photochemistry of heavy atoms and ions, and a more realistic de-  
148 scription of heating efficiencies. This model is described in detail by Koskinen  
149 et al. (2012) (hereafter, Paper I). We also used results from a state-of-the-art  
150 photochemical model (Lavvas et al., *in preparation*) to constrain the density  
151 profiles of the observed species in the lower atmosphere. We discuss the im-  
152 plications of our results in the context of different observations, and show  
153 that observations of the upper atmosphere also yield valuable constraints on  
154 the properties of the lower atmosphere.

## 155 2. Methods

### 156 2.1. Stellar emission lines

157 The interpretation of the FUV transit measurements relies on accurate  
158 characterization of the stellar emission lines and, provided that the ISM is

159 optically thick over parts of the line profile, their absorption by the ISM. The  
 160 observed transit depths also depend on stellar variability. In this section we  
 161 discuss the properties of the line profiles, stellar variability, and absorption  
 162 by the ISM. The properties of the H Lyman  $\alpha$  and the O I 1304 Å triplet  
 163 lines (hereafter, the O I lines) have been discussed in detail before (e.g.,  
 164 Ben-Jaffel and Hosseini, 2010; Koskinen et al., 2010a), and we present only  
 165 a brief summary of them here. However, the COS observations of the C  
 166 II 1335 Å multiplet (hereafter, the C II lines), and the Si III 1206.5 Å line  
 167 (hereafter, the Si III line) (Linsky et al., 2010) have not been modeled before,  
 168 and thus we constructed emission line models for these lines based on the new  
 169 data. These, and the previous models for the H Lyman  $\alpha$  and O I lines, were  
 170 used to calculate the predicted transit depths in Section 3. The observed  
 171 line-integrated transit depths for HD209458b are listed in Table 2.

### 172 *2.1.1. H Lyman $\alpha$ and O I 1304 Å lines*

173 Wood et al. (2005) measured the H Lyman  $\alpha$  emission line of HD209458  
 174 by using the high resolution echelle E140M grating on STIS, and used the  
 175 details of the line profile to constrain the column density of H in the ISM  
 176 along the line of sight (LOS) to HD209458. Following K10, we adopted the  
 177 reconstructed line profile and ISM fit parameters from Wood et al. (2005) for  
 178 the transit depth calculations in this paper. The short-term variability of the  
 179 H Lyman  $\alpha$  emissions from HD209458 was estimated by Ben-Jaffel (2007)  
 180 who used the G140M data to derive a magnitude of  $\sim 8.6 \pm 5.6$  % for this

181 variability – although the large uncertainty of the observations makes it diffi-  
182 cult to separate variability from noise. There are no observations to constrain  
183 the long-term variability or center-to-limb variations of the Lyman  $\alpha$  line on  
184 HD209458. However, typical solar characteristics provide some guidance on  
185 these properties.

186 Woods et al. (2000) studied the variability of solar Lyman  $\alpha$  emissions  
187 based on satellite observations spanning four and a half solar cycles between  
188 1947 and 1999. They found that the variability ranges between 1 and 37  
189 % during one period of solar rotation (27 days), and the average variability  
190 during one solar rotation was found to be  $9 \pm 6$  %. This result agrees well  
191 with the estimated variability of the Lyman  $\alpha$  emissions from HD209458. The  
192 rotation period of HD209458 is estimated to be  $\sim 10$ –11 days (Silva-Valio,  
193 2008). The G140M observations covered three different transits and took  
194 place within a month and a half. Each observation covered approximately  
195 2 hours in time. Thus the data can be affected by short-term variability  
196 and it is essential that such variability be properly accounted for. For this  
197 reason, we compare our models with the results of Ben-Jaffel (2007, 2008)  
198 and Ben-Jaffel and Hosseini (2010) who analyzed the data in the time tag  
199 mode and accounted for variability before calculating transit depths.

200 Short-term variability in the H Lyman  $\alpha$  line is mostly related to plage  
201 activity that is modulated by solar rotation while long-term variability de-  
202 pends on variations in both plage and active network regions (Woods et al.,  
203 2000). In fact, it is misleading to imagine the transits in any of the FUV emis-

204 sion lines as the planet crossing a smooth, uniformly emitting disk. Rather,  
 205 one has to imagine the planet crossing a relatively dark disk with scattered  
 206 bright regions. For instance, during solar maximum the plages<sup>2</sup> cover ap-  
 207 proximately 23 % of the solar disk while active network covers about 8.5 %.  
 208 The brightness contrasts of the plages and active network are 6.7 and 3.2,  
 209 respectively, when compared to the quiet sun (Worden et al., 1998; Woods  
 210 et al., 2000). This means that the transit depth in the H Lyman  $\alpha$  can vary  
 211 by factors of 0.4–3 as a function of time during maximum activity. Similar  
 212 variability can be expected in the other FUV emission lines.

213 The transit depth depends mostly on the path of the planet across the  
 214 stellar disk although the plage and active network coverage can also change  
 215 slightly with stellar rotation during the transit. This highlights the impor-  
 216 tance of light curve analysis to work out transit depths – limited ‘snapshots’  
 217 during transit may be corrupted by the planet either covering or not cover-  
 218 ing an active region. However, it is also possible for the transit depth to be  
 219 altered even if the variations are not immediately evident in the light curves.  
 220 This complicates the analysis of the observations, and underlines the need  
 221 for repeated observations at different times. We note that the plage and  
 222 active network coverage is significantly smaller during solar minimum than  
 223 it is during solar maximum. This means that the transit depth is likely to  
 224 be more stable and closer to the true transit depth during stellar minimum.

---

<sup>2</sup>We include enhanced network in the definition of a plage here.

225 Unfortunately, the activity cycle of HD209458 has not been studied in detail,  
226 and thus we have no information about it.

227 As we noted above, the properties of the O I lines were discussed exten-  
228 sively by K10 who fitted parameterized solar line profiles (Gladstone, 1992)  
229 to the O I lines of HD209458 that were observed with the STIS E140M grat-  
230 ing (Vidal-Madjar et al., 2004). We adopted the O I line profile and ISM  
231 parameters from K10 for this study, and do not discuss these properties fur-  
232 ther here. We note that the plage and active network contrasts of the O  
233 I lines are 4.2 and 1.7, respectively (Woods et al., 2000). These values are  
234 slightly smaller than the corresponding values for H Lyman  $\alpha$ . We note that  
235 limb darkening or brightening can also affect the observed transit depths  
236 (K10, Schlawin et al., 2010). However, center-to-limb variations are not par-  
237 ticularly significant in the solar H Lyman  $\alpha$  and O I lines (Curdt et al., 2008;  
238 Roussel-Dupre, 1985).

### 239 *2.1.2. C II 1335 Å and Si III 1206.5 Å lines*

240 Linsky et al. (2010) used the medium resolution ( $R \sim 17,500$ ) G130M  
241 grating of the COS instrument to observe four transits of HD209458b between  
242 September 19 and October 18, 2009 at wavelengths of 1140–1450 Å. During  
243 each HST visit, they observed the star during transit, at first quadrature,  
244 secondary eclipse and second quadrature. In order to obtain the out-of-  
245 transit reference spectra, they co-added the secondary eclipse and quadrature  
246 observations from all four visits. They also co-added the in-transit spectra

247 from all visits to create a single spectrum. The detections of the transits in  
 248 the C II 1335 Å and Si III 1206.5 Å lines were compared with observations  
 249 of other lines such as Si IV 1395 Å in which the transit was not detected.  
 250 We note that the transit in the Si III line was not detected earlier by Vidal-  
 251 Madjar et al. (2004). However, these authors use a wider wavelength interval  
 252 to calculate the line-integrated transit depth and yet report a  $2\sigma$  upper limit  
 253 of 5.9 %, implying that the  $3\sigma$  upper limit includes the transit depth observed  
 254 by Linsky et al. (2010). As we have seen, stellar variability can also cause  
 255 changes in the perceived transit depth. Therefore we are not convinced of  
 256 the reality of a non-detection in the earlier STIS G140L observations.

257 In order to calculate transit depths in the C II and Si III lines, we created  
 258 models for the stellar emission line profiles. We note that Ben-Jaffel and  
 259 Hosseini (2010) also modeled the C II lines in order to fit the transit depth  
 260 in the low resolution G140L data (Vidal-Madjar et al., 2004) where the main  
 261 components of the C II multiplet are unresolved. Their model line profiles  
 262 were also constrained by the high resolution STIS E140M observations of  
 263 Vidal-Madjar et al. (2003) that resolve the components, although this data  
 264 has low S/N and it was not used for transit observations. Here we use the  
 265 higher S/N COS observations that also resolve the main components of the  
 266 C II lines to constrain the line profile models.

267 The atomic line parameters for the C II and Si III lines are listed in  
 268 Table 1. The C II multiplet consists of three separate emission lines. The  
 269 two lines at 1335.66 Å and 1335.71 Å (hereafter, the C II 1335.7 Å line) are

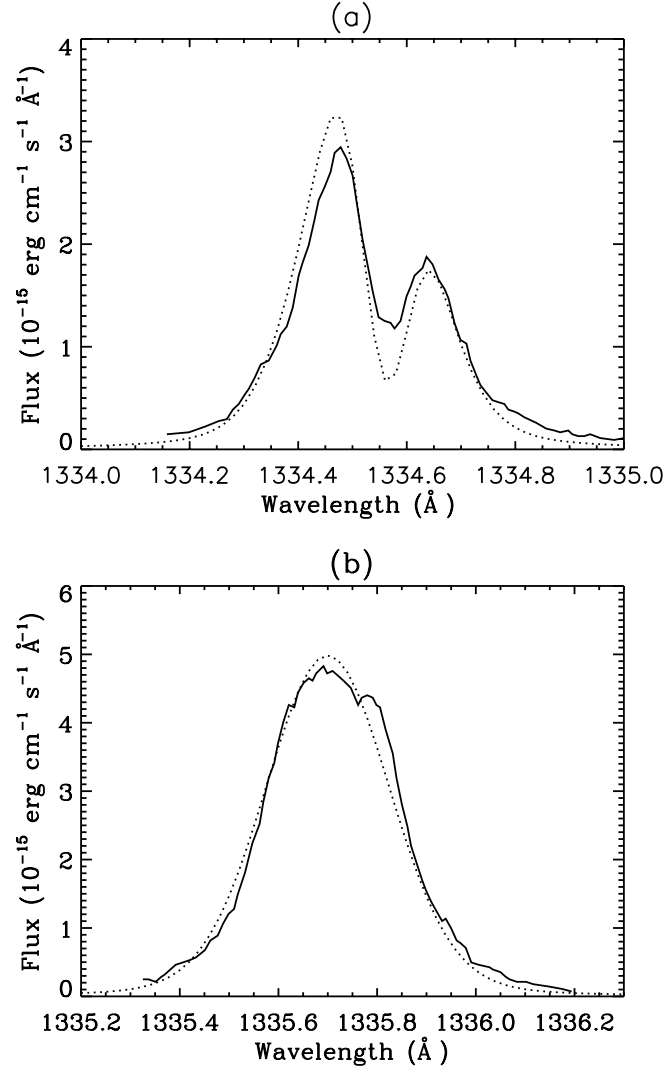


Figure 1: (a) The C II 1334.5 Å line of HD209458 (solid line, Linsky et al., 2010) fitted with a Voigt profile (see Table 1) and adjusted for absorption by the ISM (dotted line). We assumed that the column density of ground state  $\text{C}^+$  in the ISM is  $2.23 \times 10^{19} \text{ m}^{-2}$ . The relative velocity of the ISM with respect to Earth is  $-6.6 \text{ km s}^{-1}$  and the effective thermal velocity along the LOS to the star is  $12.3 \text{ km s}^{-1}$  (Wood et al., 2005). (b) The C II 1335.7 Å line of HD209458 fitted with a Voigt profile. Absorption by the ISM was assumed to be negligible. The model profiles were convolved to a spectral resolution of  $R = 17,500$ .

270 unresolved in the COS (and most solar) observations. The core of the C II  
 271 1334.5 Å line is strongly absorbed by the ISM whereas the C II 1335.7 Å line  
 272 is not similarly affected. The ground state  $^2P_{1/2,3/2}$  of C<sup>+</sup> is split into two  
 273 fine structure levels. Interstellar absorption of the C II 1335.7 Å emissions  
 274 depends on the population of the  $^2P_{3/2}$  level in the ISM. In line with a similar  
 275 assumption regarding the excited states of O (K10), we assumed that this  
 276 population is negligible. To estimate the emission line profile from HD209458,  
 277 we fitted the solar C II 1335.7 Å line from the SUMER spectral atlas (Curd  
 278 et al., 2001) with a Voigt function and adjusted the result to agree with  
 279 observations (Linsky et al., 2010). Figure 1 shows that the model line profile  
 280 agrees reasonably well with the observed line profile. The fit parameters for  
 281 this and other relevant emission lines are listed in Table 1.

Table 1: Atomic line parameters<sup>a</sup>

Line	$\lambda_0(\text{Å})$	$f_0$	$A_0(\text{s}^{-1})$	$\Delta\lambda_D(\text{Å})^b$	$\Gamma$	$F(10^{-15} \text{ erg cm}^{-2} \text{ s}^{-1})$
C II	1334.53	0.1278	$2.393 \times 10^8$	0.12	0.266	1.16
C II <sup>c</sup>	1335.66	0.01277	$4.773 \times 10^7$	N/A	N/A	N/A
C II	1335.71	0.1149	$2.864 \times 10^8$	0.16	0.224	1.66
Si III	1206.5	1.669	$2.550 \times 10^9$	0.12	0.535	2.09

<sup>a</sup>from Morton (1991)

<sup>b</sup>The line profiles are given by  $p(\lambda) = [F/(\Delta\lambda_D\sqrt{\pi})]V(a, u)$  where  $V$  is the IDL Voigt function with  $a = \Gamma/(4\pi\Delta\lambda_D)$  and  $u = (\lambda - \lambda_0)/\Delta\lambda_D$ . The flux is given at Earth distance (47 parsec).

<sup>c</sup>The emission line merges with the C II 1335.71 Å line.

282 Strong absorption by the ISM makes fitting the C II 1334.5 Å line more  
 283 complicated than fitting the C II 1335.7 Å line. Following Ben-Jaffel and



284 Hosseini (2010), we estimated that the column density of ground state C<sup>+</sup>  
 285 in the ISM is  $2.23 \times 10^{19} \text{ m}^{-2}$  by scaling the column density of C<sup>+</sup> mea-  
 286 sured along the LOS to Capella (Wood and Linsky, 1997) to the distance of  
 287 HD209458. We fitted the solar C II 1334.5 Å line from the SUMER spectral  
 288 atlas with a Voigt profile, and used the estimated column density and the  
 289 results of Wood et al. (2005) to calculate absorption by the ISM. We then  
 290 varied the total flux within the line profile until the results agreed with the  
 291 observations of Linsky et al. (2010). As a result, we obtained a pre-ISM flux  
 292 ratio of  $[\text{C II } 1334.5 \text{ Å}]/[\text{C II } 1335.7 \text{ Å}] \sim 0.7$ , which agrees well with the solar  
 293 value (Curdt et al., 2001). The model and observed line profiles are again  
 294 shown in Figure 1. We note that the ISM is optically thick at wavelengths  
 295 between 1334.54 Å and 1335.58 Å, which correspond to Doppler shifts of 2.2  
 296 and 11.2 km s<sup>-1</sup>, respectively. However, the observed flux in this region is  
 297 not zero because of spectral line broadening in the COS instrument.

298 The C II lines are formed in the upper chromosphere and lower transi-  
 299 tion region of the solar atmosphere. Similarly with H Lyman  $\alpha$ , the brightest  
 300 emissions are associated with plage activity (e.g., Athay and Dere, 1989). The  
 301 plage and active network contrasts for the C II lines are 5.9 and 1.5, respec-  
 302 tively (Woods et al., 2000). The large spatial variability makes it difficult to  
 303 characterize center-to-limb variations. However, different solar observations  
 304 point to approximately 40 % limb brightening in the 1335.7 Å line and prob-  
 305 ably a similar variation in the 1334.5 Å line, with the intensity rising steadily  
 306 at  $\mu > 0.6$  (Lites et al., 1978; Judge et al., 2003). This brightening effect is

307 due to the broadening of the emission line in the limb.

308 The Si III line arises from a transition between the  $^1S$  ground state and  
309 the  $^1P$  excited state. Again, we fitted the Si III line profile from the SUMER  
310 spectral atlas (Curd et al., 2001) with a Voigt profile and adjusted the  
311 resulting line profile to agree with observations of HD209458 (Linsky et al.,  
312 2010). Figure 2 shows the observed and model line profiles, and the fit  
313 parameters are listed in Table 1. We assumed that the abundance of  $\text{Si}^{2+}$  in  
314 the ISM is negligible. This is supported by a lack of detectable absorption  
315 by the ISM in the observed line profile. We note that absorption by the  
316 ISM affects the interpretation of the measured transit depths only if parts of  
317 the line profile are entirely absorbed or if the properties of the ISM change  
318 between observations.

319 The solar Si III line has not been studied to the same degree as the C  
320 II lines. However, some constraints on the variability and center-to-limb  
321 variations of the Si III line have been obtained. For instance, Nicolas et al.  
322 (1977) used SKYLAB observations to study the center-to-limb variations of  
323 the Si III emissions from the quiet chromosphere. They found that the line  
324 is strongly limb-brightened. The total line intensity increased by a factor of  
325 2.4 between the disk center and  $\mu = 0.73$ , and then again by a factor of 3  
326 towards the edge of the limb. This means that the total intensity in the limb  
327 is a factor of  $\sim 7$  higher than at the disk center, and the line profile is also  
328 significantly broader at  $\mu > 0.73$  with a self-reversal that does not appear at  
329 the disk center. The Si III emissions from the Sun also exhibit strong spatial

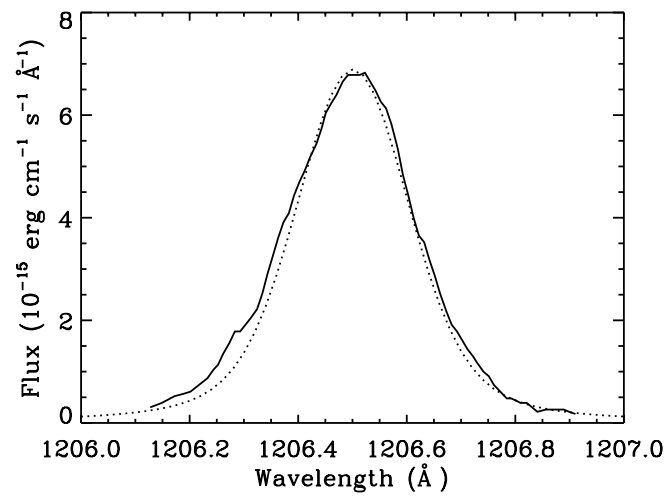


Figure 2: The Si III 1206.5 Å line of HD209458 (solid line, Linsky et al., 2010) fitted with a Voigt profile (dotted line, see Table 1). Absorption by the ISM was assumed to be negligible. The model profile was convolved to a spectral resolution of  $R = 17,500$ .

330 and temporal variability (e.g., Nicolas et al., 1982). Limb brightening makes  
 331 the transit depth appear smaller when the planet is covering the stellar disk  
 332 while a steeper transit is seen during ingress and egress (e.g., Schlawin et al.,  
 333 2010). On the other hand, if the planet covers active regions on the disk, the  
 334 transit depth can appear significantly deeper (K10).

335 Spatial variability and limb brightening of the emission lines on HD209458  
 336 can potentially be studied through a careful analysis of the transit light  
 337 curves. Ideally, the observations should be analyzed in the time tag mode  
 338 (e.g., Ben-Jaffel, 2007) to identify variations. This type of reanalysis of the  
 339 COS data is beyond the scope of this paper. Instead, we use idealized transit  
 340 depths based on a uniformly emitting stellar disk in Section 3 to show that  
 341 the optical depth of the extended thermosphere in the FUV lines is significant  
 342 and that the transit in the O I, C II, and Si III lines is comparable to the  
 343 transit in the H I line. We consider this sufficient for the present purposes.

## 344 2.2. Empirical model

345 K10 developed an empirical model to fit the UV transit observations of  
 346 HD209458b and other extrasolar planets. They argued that the H I tran-  
 347 sits can be explained in terms of three simple parameters that describe the  
 348 distribution of H in the thermosphere. These parameters are the pressure  
 349  $p_0$  where  $H_2$  dissociates (the bottom of the H layer), the mean temperature  
 350  $\bar{T}$  within the H layer and an upper *cutoff level*  $r_\infty$  based on the ionization  
 351 of H. Transits in other emission lines can be explained by fitting the abun-

352 dance of the heavier absorbers with respect to H. The details of this model  
 353 are discussed by K10 and are not repeated here. Basically it calculates the  
 354 transit depth observed at Earth orbit by assuming that the planet and its  
 355 atmosphere constitute a spherically symmetric obstacle with a density profile  
 356 in hydrostatic equilibrium up to the sonic point (when a sonic point exists).  
 357 Absorption by the ISM and spectral line broadening within the observing  
 358 instrument (STIS or COS) are taken into account. In Section 3, we compare  
 359 the transit depths calculated by the empirical model with results based on  
 360 the hydrodynamic model (see below) to show how the empirical model can  
 361 be used to fit the data and guide the development of more complex models  
 362 of the upper atmosphere.

### 363 *2.3. Hydrodynamic model*

364 We developed a one-dimensional, non-hydrostatic escape model for HD209458b  
 365 to constrain the mean temperature and ionization in the upper atmosphere  
 366 (Paper I). Results from this model demonstrate that the empirical model  
 367 is physically meaningful. It solves the vertical equations of motion for an  
 368 escaping atmosphere containing H, H<sup>+</sup>, He, He<sup>+</sup>, C, C<sup>+</sup>, O, O<sup>+</sup>, N, N<sup>+</sup>,  
 369 Si, Si<sup>+</sup>, Si<sup>2+</sup>, and electrons. The model includes photoionization, thermal  
 370 ionization, and charge exchange between atoms and ions. It calculates the  
 371 temperature profile based on the average solar X-ray and EUV (XUV) flux  
 372 and up to date estimates of the photoelectron heating efficiencies (Cecchi-  
 373 Pestellini et al., 2009, Paper I). The lower boundary of the model is at 1  $\mu$ bar

374 and thus the model does not include molecular chemistry. This is justified  
 375 because molecules are dissociated by photochemical reaction networks near  
 376 the 1  $\mu$ bar level (e.g., Garcia Munoz, 2007; Moses et al., 2011). The upper  
 377 boundary of the model is typically at 16  $R_p$ . We placed the upper boundary  
 378 at a relatively high altitude above the region of interest in this study, which  
 379 is below 5  $R_p$ . However, we do not consider the results to be necessarily  
 380 accurate above 5  $R_p$  (see Paper I for further details).

### 381 **3. Results**

#### 382 *3.1. Transit depths*

383 In this section we constrain the temperature and composition of the upper  
 384 atmosphere of HD209458b through a combined analysis of transit observa-  
 385 tions in the FUV emission lines. We also compare results from a hydrody-  
 386 namic model (see Section 2.3 and Paper I) with the empirical model of K10,  
 387 and confirm that the latter can be used to constrain the basic properties of  
 388 the density profiles in the thermosphere.

##### 389 *3.1.1. Neutral atoms*

390 K10 demonstrated that absorption by hydrogen in the extended thermo-  
 391 sphere of HD209458b explains the transits in the H Lyman  $\alpha$  line, and used  
 392 the observations to constrain the mean temperature and composition of the  
 393 thermosphere. They fitted both the line-integrated transit depth based on  
 394 the low resolution G140L data (Vidal-Madjar et al., 2004; Ben-Jaffel and

395 Hosseini, 2010), and the transit depths and light curve based on the medium  
 396 resolution G140M data (Vidal-Madjar et al., 2003; Ben-Jaffel, 2007, 2008)  
 397 (see Figures 5 and 6 of K10 for the results). The results imply that the lower  
 398 boundary of the absorbing layer of H is at  $p_0 = 0.1\text{--}1\ \mu\text{bar}$ , the mean temper-  
 399 ature within the layer is  $\bar{T} = 8,000\text{--}11,000\ \text{K}$ , and the upper boundary is at  
 400  $r_\infty = 2.7\ R_p$ . Recent photochemical calculations imply that  $\text{H}_2$  dissociates  
 401 near the  $1\ \mu\text{bar}$  level [e.g., Paper I, Moses et al. (2011)], and this is also  
 402 supported by an observational lower limit for the vertical column density of  
 403 H (France et al., 2010). Hence the mean temperature in the thermosphere  
 404 of HD209458b is approximately 8,250 K (the M7 model of K10).

405 Here we show from simple arguments that the M7 model agrees in princi-  
 406 ple with the observed H Lyman  $\alpha$  transit depth. A similar procedure can also  
 407 be used to obtain crude estimates of the transit depth for other systems, pro-  
 408 vided that the properties of the line profile and the ISM are known. Later in  
 409 this section we compare the results of the empirical model with results from  
 410 the hydrodynamic model, and show that they are consistent. To start with,  
 411 the line-integrated H Lyman  $\alpha$  transit depth of  $6.6 \pm 2.3\ \%$  (Ben-Jaffel and  
 412 Hosseini, 2010) is consistent with a 6 % transit depth at  $1215.2\ \text{\AA}$  (a Doppler  
 413 shift of  $-120\ \text{km s}^{-1}$  from the line core) i.e., the blue peak of the observed  
 414 line profile (Figure 5 of K10). Assuming that the extended atmosphere is  
 415 spherically symmetric, a 6 % transit depth measured in the blue wing (bw)  
 416 of the line profile implies an optical depth of  $\tau_{\text{bw}} \approx 1$  at the impact parameter  
 417 of  $2.1\ R_p$  from the center of the planet. Figure 3 shows the absorption cross

418 section of H in the Lyman  $\alpha$  line at a temperature of 8,250 K. The cross  
 419 section at 1215.2 Å is  $\sigma_{\text{bw}} = 2 \times 10^{-23} \text{ m}^2$  and thus a LOS column density of  
 420  $N_{\text{H}} = 5 \times 10^{22} \text{ m}^{-2}$  at 2.1  $R_p$  is required to explain the observed absorption.

421 Ekenbäck et al. (2010) and Lammer et al. (2011) argued that the optical  
 422 depth of H in the thermosphere of HD209458b is not significant and instead  
 423 a large cloud of energetic neutral atoms (ENAs) is required to explain the  
 424 H Lyman  $\alpha$  observations. In particular, Lammer et al. (2011) claimed that  
 425 a column density of  $N_{\text{H}} \approx 10^{31} \text{ m}^{-2}$  in the thermosphere is required for  
 426 strongly visible absorption. It is easy to see that this estimate is not correct  
 427 because the wings of the line profile become optically thick with column  
 428 densities much smaller than this. It also disagrees with Garcia Munoz (2007)  
 429 and Ben-Jaffel (2007, 2008) who were the first to suggest that H in the  
 430 thermosphere may be sufficiently abundant to explain the observations. This  
 431 basic result has also been confirmed by more recent calculations by Trammell  
 432 et al. (2011). All of these calculations show that the optical depth of the  
 433 thermosphere below 3  $R_p$  is not negligible.

434 The empirical model of K10 is simplified by the use of the hydrostatic  
 435 approximation. This is well justified even if the atmosphere is escaping. In  
 436 general, the density profile of the escaping gas in the thermosphere can be  
 437 estimated from (Parker, 1964):

$$n(\xi)c^2(\xi) = n_0c_0^2 \exp\left(-\int_1^\xi \frac{du}{u^2} \frac{W^2}{c^2}\right) \exp\left(-\int_1^\xi \frac{du}{c^2} v \frac{dv}{du}\right) \quad (1)$$



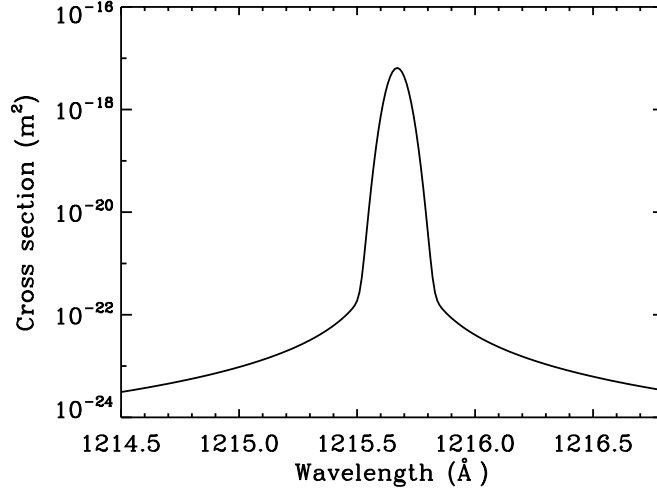


Figure 3: The absorption cross section of H in H Lyman  $\alpha$  line at  $T = 8,250$  K. Thermal and natural line broadening were modeled with a Voigt profile.

438 where  $\xi = r/r_0$ ,  $c^2(\xi) = kT(\xi)/m$ ,  $W = GM_p/r_0$ ,  $m$  is the molecular weight,  
 439 and  $v$  is the vertical flow speed. For convenience, we retained Parker's original  
 440 notation. The first integral on the right hand side of equation (1) applies in  
 441 hydrostatic equilibrium. The second integral is negligible below the sonic  
 442 point for transonic escape and always negligible for subsonic escape (i.e.,  
 443 evaporation). The sonic point on HD209458b is always above  $3 R_p$  (Paper I)  
 444 and thus the density profile of H is approximately hydrostatic at least up to  
 445  $2.1 R_p$ .

446 Assuming a hydrostatic atmosphere, the LOS column density of H at 2.1

447  $R_p$  can be estimated from:

$$N_{\text{H}}(r = 2.1 R_p) \approx n_0 \exp \left[ \frac{GM_p m}{k\bar{T}} \left( \frac{1}{r} - \frac{1}{r_0} \right) \right] \sqrt{2\pi r H(r)} \quad (2)$$

448 where  $\bar{T}$  and  $H$  are the mean temperature and scale height, respectively. We  
 449 note that the mean thermal escape parameter is:

$$\bar{X}(r) = \frac{GM_p m}{k\bar{T}r}. \quad (3)$$

450 Assuming that  $\bar{T} = 8,250$  K and using the planetary parameters of HD209458b  
 451 ( $M_p = 0.7 M_J$ ,  $R_p = 1.3 R_J$ ), we obtain values of  $\bar{X}_0 = 13.8$  and  $\bar{X}(2.1 R_p) =$   
 452 6.6. Thus, according to equation (2), the column density of  $N_{\text{H}} = 5 \times 10^{22}$   
 453  $\text{m}^{-2}$  that is required to explain the observations implies that  $n_0 = 3.5 \times 10^{17}$   
 454  $\text{m}^{-3}$ . This in turn means that  $p_0 = 0.4 \mu\text{bar}$  i.e., close to the lower boundary  
 455 of the M7 model (here the agreement with the M7 model is obviously not  
 456 exact because the transit depths in K10 are based on a complete forward  
 457 model of the observed transit within the whole line profile).

458 The parameters of the empirical model can be compared with correspond-  
 459 ing values derived from the hydrodynamic models presented in Paper I (see  
 460 Section 2.3 here for a brief summary). For instance, the mean temperature  
 461 of the empirical model corresponds roughly to the pressure-averaged temper-  
 462 ature of the thermosphere, which is given by (e.g., Holton, 2004):

$$\bar{T}_p = \frac{\int_{p_1}^{p_2} T(p) d(\ln p)}{\ln(p_2/p_1)}. \quad (4)$$

463 The hydrodynamic calculations show that the pressure averaged (mean) tem-  
 464 perature below  $3 R_p$  based on the average solar flux varies between 6,000 K  
 465 and 8,000 K for net heating efficiencies  $\eta_{\text{net}}$  between 0.1 and 1. This tempera-  
 466 ture is relatively insensitive to different assumptions about heating efficiencies  
 467 or the upper boundary conditions. In the reference C2 model of Paper I the  
 468 mean temperature is 7,200 K. This model is based on our best estimate of  
 469 the heating efficiencies that are appropriate in the strongly ionized upper  
 470 atmosphere of HD209458b.

471 With a cutoff level at  $2.7 R_p$ , we obtained a line-integrated H Lyman  $\alpha$   
 472 transit depth of 4.7 % based on the density of H in the C2 model. This  
 473 value agrees with the observations to within  $1\sigma$  (Vidal-Madjar et al., 2004;  
 474 Ben-Jaffel and Hosseini, 2010), but it is smaller than the transit depth of  
 475 6.6 % predicted by the M7 model. One reason for this is the lower mean  
 476 temperature of the C2 model. In order to facilitate a direct comparison  
 477 between the hydrodynamic model and the empirical model, we calculated the  
 478 empirical transit depth based on the mean temperature of 7,200 K (hereafter,  
 479 the M7b model). The line-integrated transit depth based on this model is  
 480 5.8 %, which is still higher than the transit depth based on the C2 model.

481 Figure 4 shows the density profiles of H,  $\text{H}^+$ , O, and  $\text{O}^+$  from the C2  
 482 model, and the density profile of H from the M7b model. The difference  
 483 between the transit depths based on the empirical and hydrodynamic models  
 484 arises because the C2 model has large temperature gradients (Paper I) and a  
 485 gradual  $\text{H}/\text{H}^+$  transition rather than a sharp cutoff. The difference does not

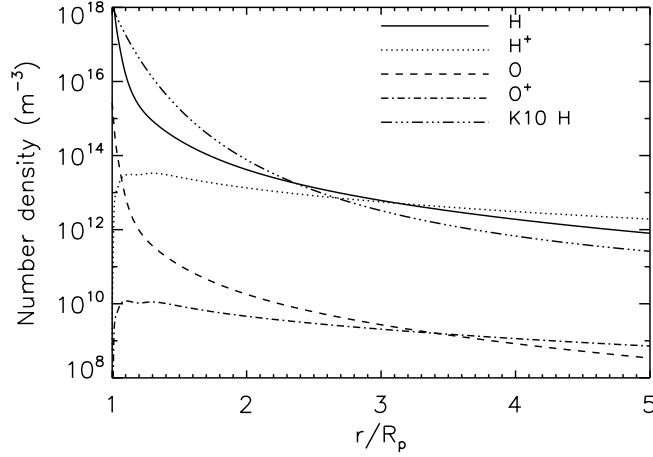


Figure 4: Density profiles O and H based on the C2 model (Paper I) and the density profile of H based on the empirical model of K10 with a mean temperature of 7,200 K.

486 arise because the density profile of the C2 model deviates from hydrostatic  
 487 equilibrium. Given the temperature gradient in the model, the density profile  
 488 is almost exactly in hydrostatic equilibrium below  $3 R_p$ . In fact, the neutral  
 489 density profile of the C2 model is better represented by a mean temperature  
 490 of 6,300 K (not shown). This implies that the correspondence of the mean  
 491 temperature of the empirical model and the pressure averaged temperature  
 492 of the hydrodynamic model is relatively good but not exact.

493 A better agreement between the transit depths based on the C2 and M7b  
 494 models is obtained with the cutoff level of the C2 model at  $5 R_p$  (see Table 2).  
 495 Figure 5 shows the line-integrated transit depth within the H Lyman  $\alpha$  line  
 496 profile as a function of the cutoff level for the C2 model. This figure indicates

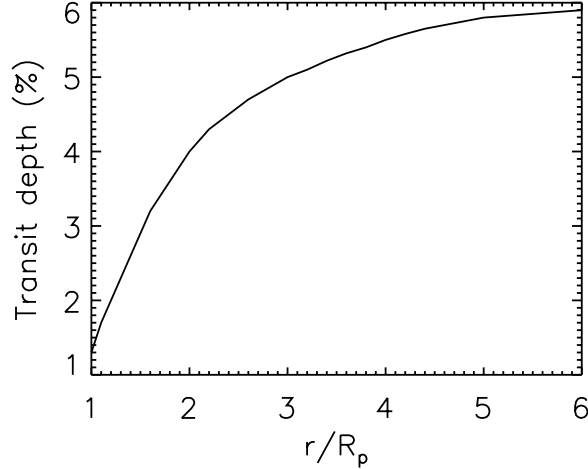


Figure 5: Line-integrated transit depth within the H Lyman  $\alpha$  line as a function of the obstacle cutoff level based on the C2 hydrodynamic model (Paper I). The K10 density profile applies to the M7b model (see text).

497 that the transit depth increases less steeply with altitude above  $4 R_p$  than  
 498 it does below this cutoff level, and saturates near  $5 R_p$ . This is a natural  
 499 consequence of the fact that the LOS column density decreases approximately  
 500 exponentially with altitude in the lower thermosphere and the wings of the  
 501 line profile become optically thin at high altitudes.

502 We note that K10 already compared the results based on the M7 model  
 503 with in-transit transmission as a function of wavelength within the H Ly-  
 504 man  $\alpha$  line profile and the light curve derived from the G140M data (Ben-  
 505 Jaffel, 2007, 2008). It is not necessary to repeat a similar comparison here  
 506 because spherically symmetric models that predict line-integrated transit

507 depths that agree with the measured values are generally compatible with  
 508 both the G140L and G140M data. This is partly because the uncertainty of  
 509 the individual data points within the line profile and the light curve is large,  
 510 and thus they do not strongly constrain the properties of the atmosphere.

511 According to Figure 4, the H/H<sup>+</sup> transition in the C2 model occurs near  
 512 3.1  $R_p$ . The exact location depends on photochemistry and vertical velocity,  
 513 and generally the transition occurs near or above 3  $R_p$  (Paper I). With a  
 514 fixed pressure at the lower boundary, a faster velocity leads to a transition  
 515 at a higher altitude. These results disagree with Yelle (2004) and Murray-  
 516 Clay et al. (2009) who predicted a lower transition altitude, but they agree  
 517 qualitatively with the solar composition model of Garcia Munoz (2007). The  
 518 density profiles of O and O<sup>+</sup> are strongly coupled to H and H<sup>+</sup> by charge  
 519 exchange. As a result, the O/O<sup>+</sup> transition occurs generally near the H/H<sup>+</sup>  
 520 transition. For instance, in the C2 model it is located near 3.4  $R_p$ . We note  
 521 that significant ionization of H and O above 3  $R_p$  is anticipated by K10 and  
 522 there is good agreement on this between the empirical and hydrodynamic  
 523 models.

524 The detection of O at high altitudes constrains the mass loss rate and  
 525 the ionization state of the upper atmosphere (see Section 3.2). However,  
 526 the large uncertainty in the observations means that repeated observations  
 527 are required to confirm the transit depth. The M7 model of K10 with a  
 528 solar O/H ratio (Lodders, 2003) yields an O I transit depth of 3.9 %, which  
 529 is within 1.5 $\sigma$  of the observed value and therefore a satisfactory fit to the

530 data. This value agrees well with the O I transit depth based on the C2  
531 model (see Table 2). K10 argued that a higher transit depth is possible if the  
532 mean temperature is higher and/or if the O/H ratio is enhanced with respect  
533 to solar. The hydrodynamic calculations indicate that the latter option is  
534 more favorable because higher temperatures lead to stronger ionization of  
535 O and may not help to significantly enhance the transit depth. Indeed, the  
536 predicted transit depth agrees with the observations to better than  $1\sigma$  if the  
537 O/H ratio is enhanced by a factor of 5 relative to solar (see the MSOL2  
538 model in Table 2).

Table 2: Model parameters and transit depths (%)

Model	$\dot{M}$ ( $10^7$ kg s $^{-1}$ )	$\eta_{\text{net}}^{\text{a}}$	$\bar{T}_p^{\text{b}}$ (K)	H I $^{\text{c}}$ $6.6 \pm 2.3^{\text{d}}$	O I $10.5 \pm 4.4$	C II 1334.5 Å $7.6 \pm 2.2$	C II 1335.7 Å $7.9 \pm 1.5$	Si III $8.2 \pm 1.4$
C1	5.6	0.56	7250	5.5	4.1	3.4	6.8	5.0
C2	4.0	0.44	7200	5.7	4.0	3.2	6.7	4.6
C3	6.4	0.57	6450	5.4	3.7	3.1	5.5	3.5
C4	4.5	0.46	7110	5.2	3.7	3.2	6.3	4.6
C5	5.6	0.56	7290	5.6	4.2	3.5	6.9	5.1
C6	3.9	0.45	7310	5.9	4.1	3.3	6.9	4.6
SOL2	11.0	0.50	7390	5.0	4.2	4.3	7.8	6.8
MSOL2	6.0	0.66	7370	5.6	7.1	5.5	10.5	8.0
M7	N/A	N/A	8250	6.6	3.9	3.9	8.0	5.8

<sup>a</sup>Net heating efficiency (see Section 2.3) i.e., the ratio of the net heating flux at all wavelengths to the unattenuated stellar flux ( $0.45 \text{ W m}^{-2}$ ) at wavelengths shorter than  $912 \text{ Å}$ .

<sup>b</sup>Pressure averaged temperature below  $3 R_p$ .

<sup>c</sup>Line-integrated transit depth. The upper boundary of the absorbing atmosphere is at  $5 R_p$  apart from the M7 model where it is at  $2.7 R_p$  for neutrals and at  $5 R_p$  for ions.

<sup>d</sup>Observed values from Ben-Jaffel and Hosseini (2010) and Linsky et al. (2010) with  $1\sigma$  errors.

539 We have now verified that the empirical model can be used to constrain  
540 the mean temperature and extent of the absorbing layer in the thermosphere

541 of HD209458b. In particular, the comparison of the empirical model with  
 542 the hydrodynamic model shows that the results of K10 were not affected  
 543 by the simplifying assumption of hydrostatic equilibrium. We note that the  
 544 purpose of the empirical model is to identify physical processes that might  
 545 otherwise be missed in more complex models that are often based on a large  
 546 number of uncertain assumptions. The results from *any* model can now be  
 547 compared with the observations by identifying the limits of the absorbing  
 548 layer and calculating the global pressure averaged temperature within that  
 549 layer. The values can then be compared with the parameters of the best-fit  
 550 empirical model.

### 551 3.1.2. Ions

552 Figure 6 shows the density profiles of the carbon and silicon ions in the  
 553 thermosphere of HD209458b based on the C2 hydrodynamic model (Paper  
 554 I). The major carbon and oxygen-bearing species in the lower atmosphere,  
 555 CO and H<sub>2</sub>O, dissociate near the 1  $\mu$ bar level (e.g., Moses et al., 2011, or  
 556 Lavvas et al., *in preparation*). Thermochemical calculations indicate that  
 557 SiO is the dominant silicon-bearing gas on HD209458b (Visscher et al., 2010).  
 558 The detection of Si<sup>2+</sup> in the upper atmosphere implies that the formation of  
 559 silicon clouds in the lower atmosphere is suppressed (see Section 3.3), and  
 560 SiO is also dissociated near 1  $\mu$ bar either thermally or by photochemistry.  
 561 Thus we assumed that only atomic carbon and silicon are present in the  
 562 thermosphere, initially with solar abundances (Lodders, 2003).



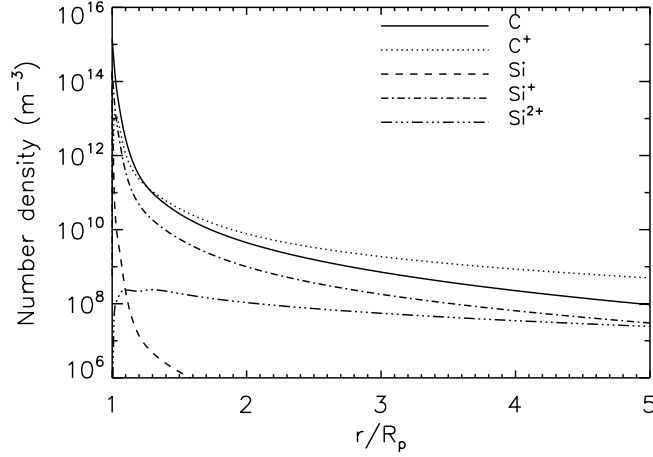


Figure 6: Density profiles of C and Si in the upper atmosphere of HD209458b based on the C2 model (Paper I).

According to Figure 6, the C/C<sup>+</sup> transition occurs at a much lower altitude of 1.2  $R_p$  than the H/H<sup>+</sup> and O/O<sup>+</sup> transitions. Silicon is also almost fully ionized at the lower boundary of the model, and the Si<sup>2+</sup>/Si<sup>+</sup> ratio is about 10 % below 3  $R_p$ . These results are in qualitative agreement with the observations, because they show that H and O are mostly neutral below 3  $R_p$  whereas C and Si are mostly ionized, and a significant abundance of Si<sup>2+</sup> is possible. However, it is also useful to explore if the results from the models are in quantitative agreement with the observations and if not, to adjust the model parameters as necessary to explain the data.

With a cutoff level at 2.7  $R_p$ , we obtained line-integrated transit depths of 2.3 %, 3.6 %, and 2.5 % in the C II 1334.5 Å, C II 1335.7 Å and Si III lines, respectively, based on the C2 model. Here we assumed that the population

575 of the  $^2P$  levels of  $C^+$  are in LTE. We also calculated empirical transit depths  
 576 based on the M7 model. In order to do this we assumed that both C and  
 577 Si are ionized at the lower boundary, and that 10 % of silicon is  $Si^{2+}$ . With  
 578 these assumptions we obtained C II 1334.5 Å and 1335.7 Å transit depths of  
 579 2.7 % and 4.2 %, respectively, and a Si III transit depth of 3 %. These values  
 580 agree well with the C2 model, and further demonstrate the consistency of  
 581 the empirical and hydrodynamic models. However, they deviate from the  
 582 observed values by more than  $2\sigma$ .

583 The cutoff level of the empirical model is somewhat arbitrary. For neutral  
 584 species it is partly based on ionization (K10), but this criterion obviously  
 585 does not apply to ions. With a cutoff level at  $5 R_p$  for the ions only, the  
 586 M7 model yields line-integrated transit depths of 3.9 %, 8 %, and 5.8 % in  
 587 the C II 1334.5 Å, C II 1335.7 Å, and Si III lines, respectively, if 40 % of  
 588 silicon is  $Si^{2+}$ . These values agree with the observed values to better than  
 589  $2\sigma$ . Similarly, by extending the cutoff level of the C2 model to  $5 R_p$ , we  
 590 obtained transit depths of 3.2 %, 6.7 %, and 4.6 % in the C II 1334.5 Å,  
 591 C II 1335.7 Å, and Si III lines, respectively (see Table 2). These values  
 592 deviate from the observed values by  $2\sigma$ ,  $0.9\sigma$ , and  $2.6\sigma$ , respectively. The  
 593 transit depths predicted by the M7 model are higher partly because the mean  
 594 temperature of 8,250 K is higher than the corresponding temperature in the  
 595 C2 model (Paper I). This also leads to the higher  $Si^{2+}/Si^+$  ratio that we used  
 596 here.

597 It is not clear if the apparent disagreement between the models and some

598 of the observations needs to be taken seriously. Stellar activity and other un-  
 599 certainties mean that the true transit depth can differ from measured values  
 600 by a significant factor (see Section 2.1). Further, the C2 model agrees with  
 601 the line-integrated H Lyman  $\alpha$  and C II 1335.7 Å transit depths to within  $1\sigma$ ,  
 602 and with the O I and C II 1334.5 Å lines to within  $2\sigma$ . Thus we could argue  
 603 that the present observations are roughly consistent with solar abundances  
 604 and heating based on the average solar XUV flux. Nevertheless, we explore  
 605 the apparent disagreement between the C2 model and the observations fur-  
 606 ther below. This disagreement is limited to the O I, C II 1334.5 Å, and Si  
 607 III lines.

608 Figure 7 shows the observed in-transit flux differences in the C II and Si  
 609 III lines as a function of wavelength together with different model predictions.  
 610 The observations indicate that the transit depths based on the C2 model fall  
 611 short of the observed values because the model underestimates the width  
 612 of the absorption lines. Linsky et al. (2010) argued that there is velocity  
 613 structure within the line profiles near Doppler shifts of  $-10 \text{ km s}^{-1}$  and  $15$   
 614  $\text{km s}^{-1}$  that accounts for broad absorption. However, the uncertainty of the  
 615 individual data points is too large to constrain the shape of the absorption  
 616 lines in detail. We agree with Linsky et al. (2010) that the presence of velocity  
 617 structure needs to be confirmed by future observations. Thus the additional  
 618 absorption could also arise from spectral line broadening.

619 We note that H<sub>2</sub> absorbs within the Si III line and it can contribute  
 620 to the observed absorption. The cross section has a lot of structure in this

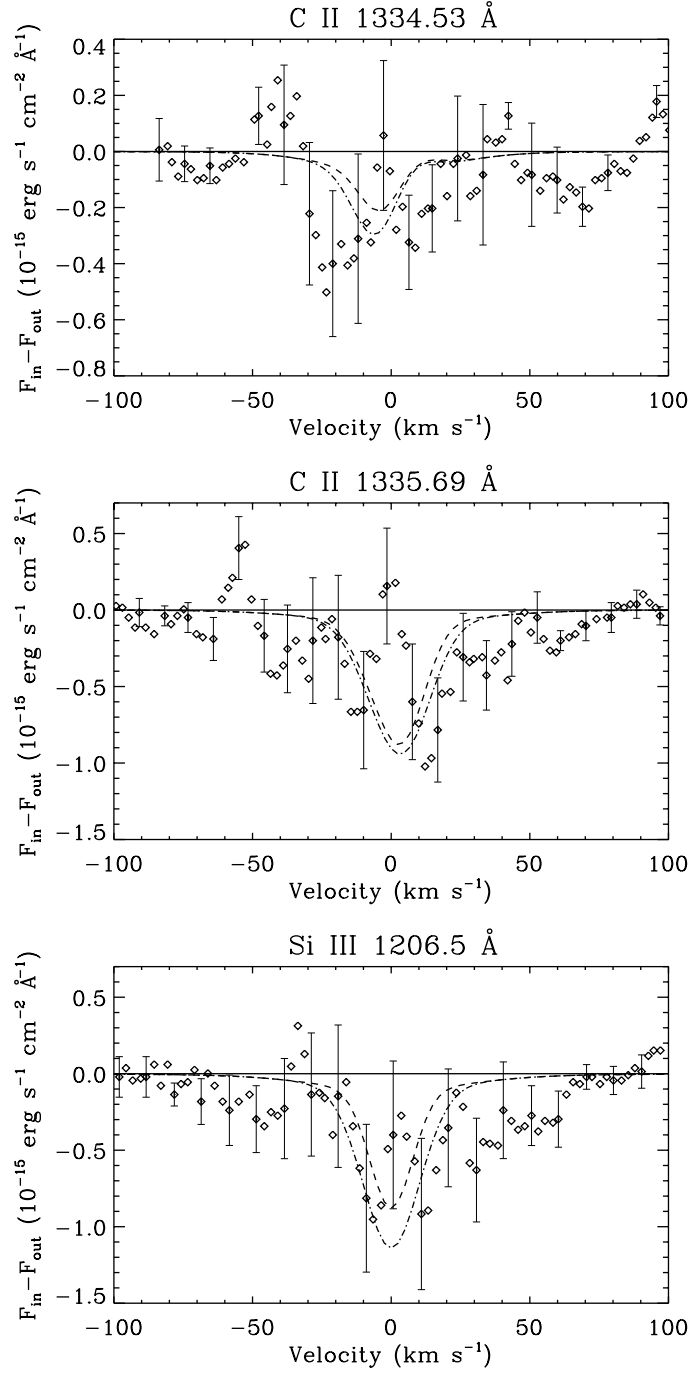


Figure 7: Flux differences between the stellar in-transit and out-of-transit C II and Si III emission lines. The data points were taken from Linsky et al.<sup>36</sup>(2010). Also shown are model predictions based on the C2 model (dashed line) and the SOL2 model (dash-dotted line). See text and Table 2 for the details of these models.

wavelength region, but for the sake of the argument we adopted a mean cross  
 section of  $\sim 2 \times 10^{-23} \text{ m}^{-2}$  (Backx et al., 1976). A transit depth of 8 % across  
 the line profile implies that the atmosphere is optically thick up to  $2.4 R_p$   
 where the LOS optical thickness is  $\tau \sim 1$ , and thus a  $\text{H}_2$  column density of  
 $5 \times 10^{22} \text{ m}^{-2}$  along this LOS would be required to explain the observed transit  
 depth. This is unrealistic because the required column density is higher than  
 the corresponding column density of H (see Section 3.1.1). Also, according  
 to our photochemical calculations  $\text{H}_2$  dissociates in the thermosphere, and  
 the mixing ratio of  $\text{H}_2$  falls below 0.1 above the  $0.1 \mu\text{bar}$  level. Such a low  
 abundance of  $\text{H}_2$  has no effect on the Si III transit depth.

A higher mean temperature leads to higher transit depths. Therefore we  
 generated a new hydrodynamic model by multiplying the average solar flux  
 by a factor of 2 and assumed a net heating efficiency of  $\eta_{\text{net}} = 0.5$  (here-  
 after, the SOL2 model). This model agrees to better than  $1\sigma$  with all of the  
 observed transit depths apart from the O I and C II 1334.5 Å lines (see Fig-  
 ure 7 and Table 2). The mean temperature of the model below  $3 R_p$  is 7,400  
 K, which is lower than the mean temperature in the M7 model. However,  
 absorption by the SOL2 model is strengthened by velocity dispersion within  
 the escaping plasma that is not included in the M7 model. In general, the  
 outflow velocity of the SOL2 model is significantly higher than the velocity  
 in the C2 model. The model also predicts a mass loss rate of  $10^8 \text{ kg s}^{-1}$ ,  
 which is twice as high as the mass loss rate based on the C2 model. This  
 proves that a higher stellar XUV flux or a corresponding alternative energy

644 source can explain the observations. An enhancement of the average solar  
645 flux by a factor of 2 is not unreasonable, and would roughly correspond to  
646 solar maximum conditions.

647 In Paper I we noted that the stellar XUV flux, or the corresponding  
648 alternative heat source, would have to be 5–10 stronger than the average  
649 solar flux to produce a mean temperature between 8,000–9,000 K. Under  
650 such circumstances, the predicted transit depths in the C II and Si III lines  
651 would obviously be even higher than the values predicted by the SOL2 model.  
652 Indeed, higher temperatures broaden absorption in the wings of the line  
653 profiles and may help to explain the in-transit flux differences better (see  
654 Figure 7). However, the energy input and temperature in the model cannot  
655 be increased without bound. Higher temperatures and flux lead to more  
656 efficient ionization of the neutral species, and as a result the transit depths  
657 in the H Lyman  $\alpha$  and O I lines begin to decrease. Also, mass loss rates of  
658  $10^9$ – $10^{10}$  kg s<sup>-1</sup> lead to the loss of 10–100 % of the planet’s mass over the  
659 estimated lifetime of the system, and this probably limits reasonable energy  
660 inputs to less than  $\sim 10$  times the solar average on HD209458b.

661 In addition to higher temperature and velocity, supersolar abundances of  
662 O, C, and Si can also lead to higher transit depths. This option is interesting  
663 because it also allows for a higher transit depth in the O I lines. As an  
664 example, we generated the MSOL2 model by enhancing the solar O/H, C/H,  
665 and Si/H abundances in the hydrodynamic model by a factor of 5. As a  
666 result, we obtained transit depths that agree with nearly all of the observed

667 line-integrated transit depths to better than  $1\sigma$  (see Table 2). However, the  
 668 MSOL2 model overestimates the line-integrated C II 1335.7 Å transit depth,  
 669 and generally overestimates absorption within the cores of the C II and Si  
 670 III lines. This could imply that a higher temperature or some other source  
 671 of additional broadening is a better explanation of the Si III and C II transit  
 672 depths while a supersolar O/H ratio is required to match the measured O I  
 673 transit depth. However, the data points in Figure 7 and the observed O I  
 674 transit depth are too uncertain and do not allow for firm constraints on this.

675     Enrichment of heavy elements is a common feature on the gas and ice  
 676 giants in the solar system. For instance, the C/H, N/H, S/H, Ar/H, Kr/H,  
 677 and Xe/H ratios in the atmosphere of Jupiter are all enriched by factors of  
 678 2–3 with respect to solar abundances (e.g., Mahaffy et al., 2000; Wong et al.,  
 679 2004). On Saturn, on the other hand, the C/H ratio is enriched by a factor  
 680 of 10 (Flasar et al., 2005; Fletcher et al., 2009). Enrichment by factors of  
 681 4–20 is expected in the N/H and S/H ratios, although condensation of NH<sub>3</sub>  
 682 and H<sub>2</sub>S in the deep atmosphere of Saturn makes it difficult to constrain the  
 683 abundances precisely (see Fouchet et al., 2009, for a review). On Neptune  
 684 and Uranus the C/H ratio is believed to be enriched by factors of 30–50  
 685 (e.g., Owen and Encrenaz, 2003; Guillot and Gautier, 2007), and similar  
 686 enrichments are possible in the abundance ratios of some of the other heavy  
 687 elements. Substantial enrichment of heavy elements with respect to solar  
 688 abundances is therefore also feasible in EGP systems even if the metallicity  
 689 of the star is close to solar.

690 Unfortunately, we cannot use the current observations to constrain the  
 691 elemental abundances of the atmosphere with accuracy. In this regard, the  
 692 large uncertainty of the observations is unfortunate, because similar observa-  
 693 tions can potentially be used to estimate them. The dissociation of molecules  
 694 at the relatively high pressure of 1  $\mu$ bar and the lack of diffusive separation  
 695 mean that the abundances of the heavy atoms and ions are simply depen-  
 696 dent on the elemental abundances and ionization rates. Observations of the  
 697 neutral species can therefore be used to constrain the temperature and ion-  
 698 ization state, and thus the elemental abundances of the heavy species, but  
 699 the S/N of the current data does not allow for strong constraints.

700 It is interesting to note that while the velocity structure of the escap-  
 701 ing plasma can lead to broader absorption that helps to explain the transit  
 702 depths, it is not necessarily detectable in the data. For instance, Figure 7  
 703 shows the transit depths based on the SOL2 model that has a relatively high  
 704 radial velocity reaching 11 km s<sup>-1</sup> by 5  $R_p$ . The velocity structure is not  
 705 detectable because the optical depth of the high velocity material is not suf-  
 706 ficient, the LOS velocity at the limb of the planet is slower than the radial  
 707 velocities in general, and because spectral line broadening within the COS  
 708 instrument smooths the structure out of the line profiles. If the presence of  
 709 velocity structure is confirmed in the data (Linsky et al., 2010), it probably  
 710 implies that there is detached, optically thick plasma moving at large veloc-  
 711 ities around the planet. If this turns out to be the case, interaction with the  
 712 stellar wind probably plays a role in giving rise to the observed absorption.



Such interaction may also produce turbulence that can broaden the absorption further (e.g., Tian et al., 2005). However, we note that non-thermal broadening such as that proposed by Ben-Jaffel and Hosseini (2010) does not appear to be necessary to explain the current observations.

### 3.2. Ionospheric escape

The escape of heavy atoms and ions has interesting consequences for the nature of the upper atmosphere. Here we discuss these consequences based on simple analytic arguments, and without explicit use of any complex models. The detection of heavy neutral species can be used to constrain the mass loss rate while the detection of heavy ions outside the atmosphere of the planet potentially constrains the strength of the planetary magnetic field. For instance, Hunten et al. (1987) derived an expression for the crossover mass limit  $m_c$  for a neutral species  $s$  to be dragged along by an escaping neutral species  $t$  of mass  $m_t < m_s$ :

$$m_c = m_t + \frac{kTF_t}{nD_{st}x_tg_0r_0^2} \quad (5)$$

where  $F_t$  is the flux ( $\text{s}^{-1} \text{sr}^{-1}$ ) of species  $t$ ,  $x_t$  is the volume mixing ratio,  $g_0$  is gravity at the lower boundary of the model region, and the mutual diffusion coefficient can be roughly estimated from:

$$nD_{st} = 1.52 \times 10^{18} \left( \frac{1}{M_s} + \frac{1}{M_t} \right)^{1/2} \sqrt{T} \quad \text{cm}^{-1}\text{s}^{-1} \quad (6)$$

730 where the masses  $M$  are in amu. We used equation (5) to estimate the mass  
731 loss rate that is required to drag neutral O to the exosphere of HD209458b.  
732 Assuming that  $x_t \sim 1$ ,  $g_0 = 10 \text{ m s}^{-1}$ ,  $r_0 = R_p$ ,  $T = 7,200 \text{ K}$ , and  $nD_{st} =$   
733  $1.3 \times 10^{22} \text{ m}^{-1}\text{s}^{-1}$ , we obtain  $F_t \approx 2.8 \times 10^{32} \text{ s}^{-1} \text{ sr}^{-1}$ . This implies a  
734 minimum mass loss rate of  $6 \times 10^6 \text{ kg s}^{-1}$ .

735 The ionosphere of HD209458b is mostly neutral below  $3 R_p$  but even weak  
736 ionization can lead to frequent Coulomb or ion-neutral collisions that enable  
737 heavy ions or atoms to escape more efficiently. In order to illustrate the role  
738 of different collisions in transporting O and  $\text{Si}^+$ , Figure 8 shows the collision  
739 frequencies for these species with H and  $\text{H}^+$  as a function of altitude based  
740 on the C2 model (Paper I). We used approximate expressions for resonant  
741 and non-resonant ion-neutral collisions, and Coulomb collisions from Schunk  
742 and Nagy (2000) to calculate the momentum transfer collision frequencies.  
743 The collision frequency between two neutral species, on the other hand, was  
744 estimated from the mutual diffusion coefficient as:

$$\nu_{st} = 5.47 \times 10^{-11} \left( \frac{1}{M_s} + \frac{1}{M_t} \right)^{-1/2} \frac{n_t \sqrt{T}}{M_s} \quad (7)$$

745 where the number density  $n_t$  is in  $\text{cm}^{-3}$ . The results indicate that the trans-  
746 port of O depends on collisions with H below  $3.5 R_p$  whereas the transport  
747 of  $\text{Si}^+$  depends on collisions with  $\text{H}^+$  at all altitudes.

748 Oxygen is the heaviest neutral species detected in the escaping atmo-  
749 sphere, and this implies that the mass loss rate from HD209458b is  $\dot{M} > 6 \times$

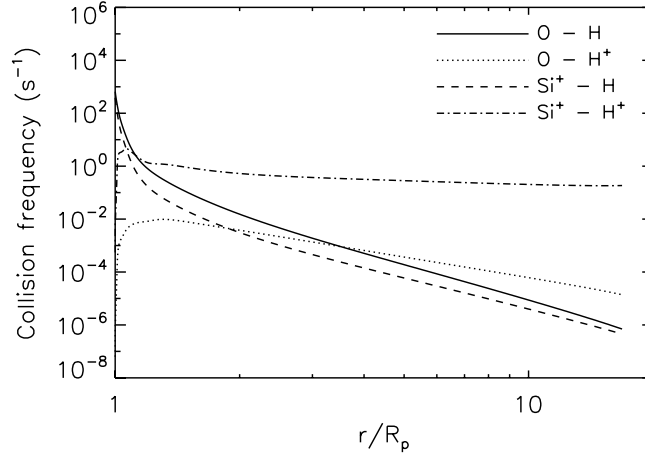


Figure 8: Momentum transfer collision frequencies based on the C2 model.

750  $10^6 \text{ kg s}^{-1}$ . This result agrees with Vidal-Madjar et al. (2003) although it  
 751 is less model-dependent and based on different criteria. The dominance of  
 752 Coulomb collisions means that the heavy ions can escape even if the mass loss  
 753 rate is lower than this. Our models predict mass loss rates of  $\dot{M} \approx 5 \times 10^7$   
 754  $\text{kg s}^{-1}$  (Table 2) and thus diffusive separation does not take place in the ther-  
 755 mosphere of HD209458b for neutral species with masses less than  $\sim 130$  amu.  
 756 We note that this is the case even if escape is subsonic. In fact, equation (5)  
 757 was originally derived for subsonic escape under the diffusion approximation  
 758 although it is also valid for supersonic escape (Zahnle and Kasting, 1986).

759 We used the collision frequencies to derive expressions for the ion fractions  
 760  $f_i = n_{\text{H}^+}/n_{\text{H}}$  at which ion-neutral and Coulomb collisions become important.  
 761 The ratio of the non-resonant neutral-ion to neutral-neutral collisions exceeds

762 10 % when

$$f_i \approx 10^{-24} \sqrt{\frac{T}{M_{si} \gamma_s e^2}} \quad (8)$$

763 where  $i$  denotes  $H^+$ ,  $s$  denotes the colliding species,  $\gamma_s$  is the neutral po-  
 764 larizability and all units are in cgs. However, the collision of O with  $H^+$  is  
 765 resonant and in this case the required ratio differs slightly from the above  
 766 expression. The ratio of the Coulomb to non-resonant ion-neutral collisions,  
 767 on the other hand, exceeds 10 % when

$$f_i \approx 4.24 \times 10^{11} \frac{T^{3/2}}{Z_s^2 Z_i^2} \sqrt{\frac{M_{sn} \gamma_n e^2}{M_{si}}}. \quad (9)$$

768 where  $i$  denotes  $H^+$  (or the dominant ion) and  $n$  is  $H$  (or the dominant  
 769 neutral). For  $Si^+$  this fraction is  $f_i \approx 10^{-4}$  (with  $\gamma_H = 6.7 \times 10^{-25} \text{ cm}^3$ ).  
 770 These equations can be used to determine if equation (5) is valid, or if more  
 771 complex plasma models are required.

772 Trammell et al. (2011) argued that HD209458b could have a strong plane-  
 773 tary magnetic field that can impede the escape of ions from equatorial regions  
 774 and restrict it to the polar regions. Although the magnetic field does not di-  
 775 rectly interfere with the escape of the neutral atoms, the trapped ions can  
 776 stop them from escaping if the neutral-ion collision frequency is sufficiently  
 777 high. Unfortunately, transit observations are not spatially resolved and they  
 778 cannot be used directly to determine if escape is limited to the poles, or if the  
 779 atmosphere is also escaping over the equator. However, the transit depths  
 780 depend on the size of the optically thick obstacle covering the star. If mass

781 loss is suppressed at low and mid-latitudes, the heavy species are no longer  
782 mixed into the upper atmosphere other than at the poles where they are  
783 allowed to escape. This means that the cross-sectional area covered by the  
784 ions shrinks and may become insufficient to explain the observations. Even if  
785 the plasma spreads to cover a larger area after being ejected from the poles,  
786 it is diluted in the process and thus it is not clear if the resulting cloud would  
787 have sufficient optical depth to be detectable.

788 Assuming that the charged particles escape the Roche lobe of the planet  
789 unimpeded at the equator, we estimated an upper limit for the planetary  
790 magnetic field by evaluating the magnetic moment that allows them to do  
791 so. In order to estimate this limit, we calculated the plasma  $\beta$  and the inverse  
792 of the second Cowling number ( $\text{Co}^{-1}$ ) below  $5 R_p$  in the C2 model from:

$$\beta = \frac{2\mu_0 p}{B^2} \quad , \quad \text{Co}^{-1} = \frac{\mu_0 \rho v^2}{B^2}$$

793 where  $v$  is the vertical velocity. Assuming a dipolar magnetic field, we ob-  
794 tained a limiting magnetic moment of  $3.2 \times 10^{25} \text{ Am}^2$  or  $0.04 m_J$  ( $m_J =$   
795  $1.5 \times 10^{27} \text{ Am}^2$  is the magnetic moment of Jupiter). This magnetic moment  
796 ensures that  $\beta > 10$  below  $5 R_p$  and that  $\text{Co}^{-1}$  reaches 10 by  $5 R_p$ . Magnetic  
797 moments of  $m_p \lesssim 0.04 m_J$  agree quite well with the scaling laws discussed  
798 by Griesmeier et al. (2004). We note that the limiting moment produces an  
799 equatorial surface field that is approximately 4 times lower than the surface  
800 field of the Earth.

### 801 3.3. *Cloud formation on HD209458b*

802 We have shown that a substantial abundance of silicon in the upper at-  
803 mosphere is required to produce a detectable transit in the Si III line. If the  
804 silicon ions originate from the atmosphere of the planet, at least a solar Si/H  
805 ratio is necessary. According to thermochemical equilibrium models, silicon  
806 should condense into clouds of forsterite ( $\text{Mg}_2\text{SiO}_4$ ) and enstatite ( $\text{MgSiO}_3$ )  
807 in the lower atmosphere of HD209458b (Visscher et al., 2010). If the forma-  
808 tion of enstatite is suppressed, silicon should condense to form quartz ( $\text{SiO}_2$ )  
809 instead. In any case, condensation is expected to remove almost all of the  
810 silicon from the upper atmosphere. The detection of  $\text{Si}^{2+}$  implies that the  
811 abundance of silicon in the thermosphere is substantial, and thus the conden-  
812 sation of silicon does not take place in the atmosphere of HD209458b. This  
813 has significant implications for the structure and dynamics of the atmosphere.

814 Sing et al. (2008a,b) analyzed the absorption line profile of Na in the  
815 atmosphere of HD209458b in detail and argued that the abundance of Na  
816 is depleted above the 1 mbar level. They suggested that this is due to the  
817 condensation of sodium into  $\text{Na}_2\text{S}$ , although ionization could not be ruled  
818 out decisively. Based on the condensation temperature of Na, they argued  
819 that the temperature in the upper atmosphere of HD209458b near 1 mbar  
820 is  $420 \pm 190$  K. This temperature is significantly lower than the outcome of  
821 typical radiative transfer models for HD209458b (e.g., Showman et al., 2009).  
822 We note that the condensation temperature of forsterite and enstatite is  
823 higher than 1,300 K at 1 mbar (Visscher et al., 2010). Because silicon clouds

do not form, the  $\text{Na}_2\text{S}$  clouds cannot form either. Further, the formation of  $\text{Na}_2\text{S}$  relies on  $\text{H}_2\text{S}$ , which is dissociated above the 1 mbar level (Zahnle et al., 2009). This implies that any depletion of Na at high altitudes is most likely due to photoionization and/or thermal ionization.

Figure 9 shows a dayside temperature (T-P) profile for HD209458b based on Showman et al. (2009). This profile is similar to the dayside temperature profile adopted by Moses et al. (2011). The figure also shows the condensation curves for forsterite and enstatite. The T-P profile crosses the condensation curve for forsterite below the 100 bar level. However, the temperature profile in the deep atmosphere is uncertain, and the current profile only barely crosses the condensation curve. Also, the formation of forsterite ties only a fraction of the total abundance of silicon into clouds (Visscher et al., 2010). However, the T-P profile crosses the condensation curves for both forsterite and enstatite in a ‘cold trap’ near 10 mbar. To prevent this, the temperature in the cold trap would have to be  $T \gtrsim 1,600$  K. This is not totally unbelievable but probably unlikely. In any case, the temperature is close enough to the condensation curves so that moderate vertical transport might be able to preserve silicon above the cold trap.

Spiegel et al. (2009) explored a range of turbulent diffusion coefficients  $K_{zz}$  that would be required to prevent the condensation of TiO and VO in the atmospheres of different EGPs, including HD209458b. In fact, they assumed that condensates form in the cold trap but are then transported to higher altitudes where they evaporate. Their work ignores the detailed chemistry

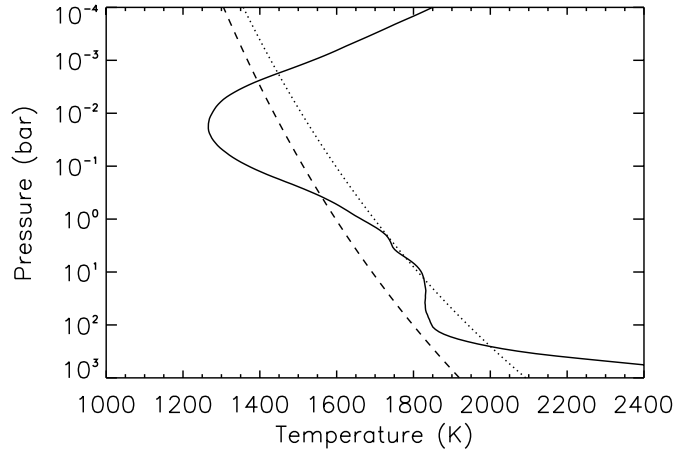


Figure 9: The dayside temperature-pressure (T-P) profile of HD209458b from Showman et al. (2009) that includes a temperature inversion at low pressures. The condensation curves for forsterite (dotted line) and enstatite (dashed line) are shown.

847 of condensation, and thus the results are simply based on the ratio of  $K_{zz}$  to  
 848 the diffusion coefficient estimated from

$$D_p \approx v_p H$$

849 where  $v_p$  is the particle settling velocity and  $H$  is the pressure scale height.  
 850 The formation of condensates is probably too complicated for such a sim-  
 851 plistic treatment, but the results provide some guidance on the value of  $K_{zz}$   
 852 that is required to lift the condensates from the cold trap.

853 We calculated  $D_p$  for forsterite grains with a radius of  $0.1 \mu\text{m}$  and density<sup>3</sup>

---

<sup>3</sup>This is the density of the material in the particles, not the density of the particles in



854 of  $3,200 \text{ kg m}^{-3}$  (Fortney et al., 2003; Cooper et al., 2003). The settling  
 855 velocity for such particles in the cold trap is  $v_p \approx 3 \times 10^{-3} \text{ m s}^{-1}$  and  
 856  $D_p \approx 2 \times 10^3 \text{ m}^2 \text{ s}^{-1}$ . Given that the upper edge of the cold trap is near the  
 857 1 mbar level where  $D_p$  is higher,  $K_{zz} \gtrsim 10^5 \text{ m}^2 \text{ s}^{-1}$  is sufficient to prevent the  
 858 settling of the cloud particles in the lower atmosphere. We note that mass  
 859 loss does not help to enhance the mixing of the particles at low altitudes  
 860 significantly. The vertical velocity based on the mass loss rate of  $10^7 \text{ kg s}^{-1}$   
 861 is only  $4.8 \times 10^{-7} \text{ m s}^{-1}$  at 10 mbar and  $8 \times 10^{-3} \text{ m s}^{-1}$  at  $1 \mu\text{bar}$ .

862 Estimating  $K_{zz}$  on extrasolar planets is very difficult, partly because there  
 863 is no agreement on exactly what physical processes this parameter describes  
 864 even in much more sophisticated solar system applications. The most recent  
 865 estimates for HD209458b are based on assuming that  $K_{zz} \sim \bar{v}H$  where  $\bar{v}$   
 866 is the rms vertical velocity from circulation models (e.g., Showman et al.,  
 867 2009). Based on the GCMs of Showman et al. (2009) and an assumed den-  
 868 sity dependence with altitude, Moses et al. (2011) estimated that the high  
 869 pressure value of  $K_{zz} = 10^6 \text{ m}^2 \text{ s}^{-1}$ , which implies that  $K_{zz} \gtrsim 10^7 \text{ m}^2 \text{ s}^{-1}$   
 870 at  $p \lesssim 10 \text{ mbar}$ . If such high values are realistic, turbulent mixing is almost  
 871 certain to prevent the settling of the condensates and to preserve gaseous  
 872 silicon in the upper atmosphere.

873 We note that the above requirements on the value of  $K_{zz}$  may in fact be  
 874 overestimated because they are based on the assumption that clouds particles

---

the atmosphere.

875 form in the cold trap. Cloud formation has to be studied in the context of  
 876 a photochemical model that includes the chemistry of condensation. If the  
 877 chemical timescale is longer than the transport timescale, the cloud droplets  
 878 may not form in the first place before the gas escapes from the cold trap.  
 879 Also, the temperature structure near the cold trap needs to be constrained in  
 880 greater detail. The formation of condensates is a complex problem that will  
 881 be studied in future work (Lavvas et al., *in preparation*) in order to better  
 882 constrain the required values of  $K_{zz}$ . For our purposes it is sufficient to note  
 883 that the current estimates of  $K_{zz}$  imply, in agreement with the observations,  
 884 that silicon clouds do not form in the upper atmosphere of HD209458b.

#### 885 4. Discussion and Conclusions

886 We have used multiple observational constraints and theoretical models  
 887 to characterize the upper atmosphere of HD209458b. Contrary to many of  
 888 the earlier studies, we did not treat the thermosphere independently of the  
 889 rest of the atmosphere. In fact, we have shown that observations of the upper  
 890 atmosphere can be used to obtain useful constraints on the characteristics  
 891 of the lower atmosphere. This is important because the extended upper  
 892 atmospheres of close-in EGPs produce much larger transit depths than those  
 893 arising from the lower atmosphere. In this work, we concentrated mostly on  
 894 the FUV transit measurements. Future work should explore the possibility  
 895 of extending the range of possible observations to other wavelength regions,  
 896 as well as obtaining repeated observations in the FUV lines. Theoretical

models should be developed to support new observations and to clarify the interpretation of the existing data.

In agreement with K10, we showed that the H Lyman  $\alpha$  transit observations (Vidal-Madjar et al., 2003, 2004; Ben-Jaffel, 2007, 2008; Ben-Jaffel and Hosseini, 2010) can be fitted with a layer of H in the thermosphere that is described by three simple parameters. These are the pressure at the bottom of the H layer, the mean temperature in the thermosphere, and a cutoff level due to ionization. The most important parameters are the pressure at the lower boundary and the mean temperature. Because H is the dominant species in the thermosphere, the data can be used to estimate the temperature of the thermosphere. Choosing a lower boundary pressure of 1  $\mu$ bar based on the location of the H<sub>2</sub>/H dissociation front in recent photochemical models (Moses et al., 2011) and observational constraints (France et al., 2010), we measured a mean temperature of about 8,250 K in the thermosphere below 3  $R_p$ . However, the uncertainty of the observations is large, and the  $1\sigma$  upper and lower limits on this temperature are approximately 6,000 K and 11,000 K, respectively<sup>4</sup>.

We used a hydrodynamic model that treats the heating of the upper atmosphere self-consistently and the average solar XUV spectrum (Paper I) to show that a mean temperature of 8,250 K in the upper atmosphere below 3  $R_p$  is higher than the maximum temperature allowed by stellar heating.

---

<sup>4</sup>This uncertainty does not include the possible uncertainties in the other parameters of the fit.

918 Given that a net heating efficiency equal to or higher than 100 % is unrealis-  
 919 tic, this temperature requires either a non-radiative heat source, additional  
 920 opacity, or it implies that the XUV flux of HD209458 is higher than the  
 921 corresponding solar flux. Interestingly, this would also imply that the mass  
 922 loss rate could be higher by a factor of 2 or more than previously anticipated  
 923 (e.g., Paper I). However, the uncertainty in the H Lyman  $\alpha$  observations also  
 924 allows for a slightly lower temperature of 7,200 K that is typical of stellar  
 925 heating based on the average solar XUV flux and our best estimate of the  
 926 net heating efficiency. Therefore the temperature implied by the H Lyman  $\alpha$   
 927 observations and the mean temperature of the basic hydrodynamic models  
 928 are in good agreement.

929 We note that the temperature in the lower thermosphere near the 1  $\mu$ bar  
 930 region has been constrained previously by Vidal-Madjar et al. (2011a,b) who  
 931 used the Na D lines to constrain the density and temperature profiles in the  
 932 atmosphere of HD209458b. Their results point to a temperature of  $\sim 3,600$   
 933 K that is actually higher than the temperature at the lower boundary of  
 934 our hydrodynamic model and consistent with a high mean temperature at  
 935 lower pressures in the thermosphere. However, we caution the reader that  
 936 the temperature profile based on the Na D lines may not be accurate. This is  
 937 because Vidal-Madjar et al. (2011a) used a simple expression for the optical  
 938 depth due to Na that is based on the scale height of the atmosphere [their  
 939 equation (1)]. This expression is only valid if Na is uniformly mixed with  
 940 H<sub>2</sub>. Since the authors also argue that Na is depleted (i.e., its mixing ratio

941 changes with altitude) above  $\sim 10$  mbar, its density scale height cannot be  
942 used to estimate temperatures accurately.

943 The detection of O in the thermosphere allowed us to constrain the mass  
944 loss rate from HD209458b based on the crossover mass concept formulated  
945 by Hunten et al. (1987). This is because O is transported to high altitudes  
946 in the upper atmosphere primarily by collisions with H. We found that a  
947 minimum mass loss rate of  $6 \times 10^6 \text{ kg s}^{-1}$  is required to prevent the diffusive  
948 separation of O. This is one of the most reliable constraints on the mass  
949 loss rate available at present. Our hydrodynamic calculation based on the  
950 average solar XUV flux predicts a mass loss rate close to  $5 \times 10^7 \text{ kg s}^{-1}$ .  
951 This implies that species with a mass up to  $\sim 130$  amu are uniformly mixed  
952 in the thermosphere. Similar constraints do not apply to heavy ions. They  
953 are transported to high altitudes by Coulomb collisions with  $\text{H}^+$  that are  
954 much more efficient in preventing diffusive separation compared to collisions  
955 of neutral atoms with H.

956 In agreement with K10, we found that the presence of O with a solar abun-  
957 dance and a temperature based on the H Lyman  $\alpha$  measurements explains  
958 the transits observed in the O I lines. Our models predict a line-integrated  
959 transit depth of approximately 4 % that deviates from the measured transit  
960 depth by  $1.5\sigma$  and thus agrees with the uncertainty of the observations. How-  
961 ever, the predicted transit depths fall systematically short of the measured  
962 value. K10 suggested that a higher transit depth is possible if the O/H ratio  
963 is supersolar, the temperature of the thermosphere is higher than expected,

964 and/or the observations probe escaping gas outside the Roche lobe of the  
965 planet, and we agree with their conclusions. As we explain below, we found  
966 that the same is true for the other heavy species.

967 In order to calculate predicted transits in the C II and Si III lines, we  
968 created model emission line profiles for HD209458 based on SUMER ob-  
969 servations of the Sun (Curdt et al., 2001) adjusted to the observations of  
970 HD209458 (Linsky et al., 2010). We did not find evidence for significant ab-  
971 sorption by the ISM in the C II 1335.7 Å or the Si III line. Parts of the C II  
972 1334.5 Å line, on the other hand, are optically thick in the ISM and we took  
973 this into account in our models. We note that resolved observations of the  
974 emission line profiles can be used to characterize the composition of the ISM  
975 and the activity of the host star. This information is a valuable byproduct  
976 of the FUV transit observations that typically need to be repeated several  
977 times.

978 With solar abundances, the same models that agree with the H Lyman  $\alpha$   
979 transit observations tend to underestimate the transit depths in the C II  
980 and Si III lines. Similarly with the O I lines, higher transit depths in the C  
981 II and Si III lines are possible if the mean temperature of the absorbers is  
982 higher than expected and/or the C/H and Si/H ratios are supersolar. With  
983 solar abundances, a  $1\sigma$  agreement with the observed line-integrated transit  
984 depths is possible if the stellar XUV flux (or the stellar flux combined with  
985 an additional heat source) is higher than or equal to 2 times the average  
986 solar XUV flux. This corresponds to typical solar maximum conditions,

987 and it is quite interesting that a similar enhancement may be required to  
988 explain the relatively high mean temperature in the thermosphere that we  
989 estimated earlier. Alternatively, with heating based on the average solar  
990 flux, an agreement with the observations is possible with the O/H, C/H and  
991 Si/H enhanced by a factor of  $\sim 3\text{--}5$  relative to solar abundances (Lodders,  
992 2003). In any case, the atmosphere is escaping with a minimum mass loss  
993 rate given above. This is evident because of both the high temperature of  
994 the thermosphere and the detection of heavy species at high altitudes.

995 We note that the transit observations are affected by stellar variability  
996 that can lead to significant changes in the observed transit depths. Spatial  
997 variations of intensity on the stellar disk during maximum activity or limb  
998 brightening may render the transit occasionally undetectable, or enhance  
999 it by a significant factor. Generally, observations obtained during periods  
1000 of minimum activity are more reliable. Ben-Jaffel (2007) characterized the  
1001 short-term variability of HD209458 in the H Lyman  $\alpha$  line, but the variabil-  
1002 ity of the O I, C II, and Si III are poorly characterized. This introduces  
1003 an additional element of uncertainty into the transit depths that needs to  
1004 be constrained by repeated observations of the star and the transits in the  
1005 FUV lines. It also means that the qualitative explanation of the present ob-  
1006 servations that is based on heating by the average solar XUV flux and solar  
1007 abundances (Paper I) may be sufficient even if the predicted transit depths  
1008 in the O I, C II, and Si III lines do not exactly match the current measure-  
1009 ments. On the other hand, if higher transit depths are confirmed, they can

1010 be used to further constrain the mean temperature and abundances as we  
1011 have shown.

1012 The detection of heavy ions escaping the atmosphere can potentially be  
1013 used to constrain the magnetic field strength of the planet. We estimated an  
1014 upper limit of  $0.04 m_J$  for the magnetic moment that allows the heavy ions  
1015 to escape unimpeded at the equator. The estimated magnetic moment agrees  
1016 with the scaling laws for the magnetic field strengths of tidally locked close-in  
1017 EGPs by Griesmeier et al. (2004). On the other hand, a strong magnetic field  
1018 inhibits the flow of ions from the equator and may only allow for escape at the  
1019 poles (e.g., Trammell et al., 2011). If the neutral-ion collision frequencies are  
1020 sufficient, the trapped ions may also prevent the neutral atoms from escaping.  
1021 We note that a uniform upward flux is required to mix the atmosphere, and  
1022 escape at the poles may not be sufficient to create a large enough obstacle to  
1023 explain the transits in the O I, C II, and Si III lines. Detailed models of the  
1024 magnetosphere that include the heavy species are required to assess if this is  
1025 the case or not.

1026 The detection of  $\text{Si}^{2+}$  in the upper atmosphere means that silicon can-  
1027 not condense to form enstatite, forsterite, or other condensates in the lower  
1028 atmosphere. This is clear because at least a solar abundance of silicon in  
1029 the thermosphere is required to explain the large transit depth in the Si III  
1030 line. According to the calculated temperature profiles for HD209458b (e.g.,  
1031 Showman et al., 2009), condensation is expected in a cold trap near the 10  
1032 mbar level. Provided that the temperature is not much higher than expected



1033 near the cold trap, efficient mixing is required to prevent condensation. Fol-  
 1034 lowing an argument similar to that of Spiegel et al. (2009), we estimated  
 1035 that an eddy mixing coefficient of  $K_{zz} \gtrsim 10^5 \text{ m}^2 \text{ s}^{-1}$  below 1 mbar is suffi-  
 1036 cient to prevent the condensation of forsterite and enstatite in the cold trap.  
 1037 We note that much higher values than  $10^5 \text{ m}^2 \text{ s}^{-1}$  were assumed by recent  
 1038 photochemical models by Garcia Munoz (2007) and Moses et al. (2011).

1039 A stratospheric temperature inversion may also be necessary to suppress  
 1040 condensation. This is because the cold trap cannot extend to much lower  
 1041 pressure than 1 mbar or the required values of  $K_{zz}$  become too high. Also,  
 1042 the lack of condensation implies that the temperature of the lower atmosphere  
 1043 should be relatively high. The detection of silicon in the upper atmosphere  
 1044 thus provides further evidence for a stratosphere on HD209458b that was  
 1045 first proposed by Knutson et al. (2008). We note that existing radiative  
 1046 transfer models do not account for molecular opacity at UV wavelengths or  
 1047 visible absorbers potentially generated by photochemistry (e.g., Zahnle et al.,  
 1048 2009). Our results provide motivation for more detailed models of thermal  
 1049 structure below the thermosphere that can constrain the chemistry of the  
 1050 lower atmosphere. Once this is achieved, better constraints on the dynamics  
 1051 can be derived.

1052 We also address an old problem related to the atmosphere of HD209458b.  
 1053 Based on the observed transits in the Na D lines, Charbonneau et al. (2002)  
 1054 argued that Na is depleted in the atmosphere because their cloudless so-  
 1055 lar composition model predicted significantly deeper absorption in the D

lines. In addition to photoionization, molecular chemistry, and low primordial abundance of Na, they suggested that the formation of high altitude clouds can explain the observed depletion. Later Sing et al. (2008a,b) found further evidence for the depletion of Na above the 3 mbar level, and argued that condensation of  $\text{Na}_2\text{S}$  is the most likely explanation. The fact that silicon does not condense implies that condensation of  $\text{Na}_2\text{S}$  is also unlikely. The observed depletion is therefore most likely due to photoionization and/or thermal ionization. However, the density profile and ionization state of Na should be studied in the context of molecular and ion chemistry below the 0.1  $\mu\text{bar}$  level to verify that this is the case.

We thank H. Menager, M. Barthelemy, N. Lewis, and D. S. Snowden for useful discussions and correspondence, and A. Showman and N. Lewis for sharing some of their temperature profiles. We also acknowledge the "Modeling atmospheric escape" workshop at the University of Virginia and the International Space Science Institute (ISSI) workshop organized by the team "Characterizing stellar and exoplanetary environments" for interesting discussions and an opportunity to present our work. The calculations for this paper relied on the High Performance Astrophysics Simulator (HiPAS) at the University of Arizona, and the University College London Legion High Performance Computing Facility, which is part of the DiRAC Facility jointly funded by STFC and the Large Facilities Capital Fund of BIS. SOLAR2000

1079 Professional Grade V2.28 irradiances are provided by Space Environment  
1080 Technologies.

## 1081 **References**

1082 Athay, R. G., Dere, K. P., 1989. Temperature and center-limb variations of  
1083 transition region velocities. *Astrophys. J.*, 346, 514–522.

1084 Backx, C., Wight, G. R., Van der Wiel, M. J., 1976. Oscillator strengths  
1085 (10–70 eV) for absorption, ionization and dissociation in H<sub>2</sub>, HD and D<sub>2</sub>,  
1086 obtained by an electron–ion coincidence method. *J. Phys. B: Atom. Molec.*  
1087 *Phys.*, 9, 315–331.

1088 Beaulieu, J. P., et al., 2010. Water in the atmosphere of HD209458b from  
1089 3.6–8  $\mu$ m IRAC photometric observations in primary transit. *Mon. Not.*  
1090 *R. Astron. Soc.*, 409, 963–974.

1091 Ben-Jaffel, L. 2007. Exoplanet HD209458b: Inflated hydrogen atmosphere  
1092 but no sign of evaporation. *Astrophys. J. Lett.*, 671, L61–L64.

1093 Ben-Jaffel, L. 2008. Spectral, spatial, and time properties of the hydrogen  
1094 nebula around exoplanet HD209458b. *Astrophys. J.*, 688, 1352–1360.

1095 Ben-Jaffel, L., Hosseini, S. S., 2010. On the existence of energetic atoms in  
1096 the upper atmosphere of exoplanet HD209458b. *Astrophys. J.*, 709, 1284–  
1097 1296.

1098 Brown, T. M., Charbonneau, D., Gilliland, R. L., Noyes, R. W., Burrows,  
1099 A., 2001. Hubble Space Telescope time-series photometry of the transiting  
1100 planet of HD209458. *Astrophys. J.*, 552, 699–709.

1101 Cecchi-Pestellini, C., Ciaravella, A., Micela, G., Penz, T., 2009. The relative  
1102 role of EUV radiation and X-ray in the heating of hydrogen-rich exoplanet  
1103 atmospheres. *Astron. Astrophys.*, 496, 863–868.

1104 Charbonneau, D., Brown, T. M., Latham, D. W., Mayor, M., 2000. Detection  
1105 of planetary transits across a Sun-like star. *Astrophys. J. Lett.*, 529, L45–  
1106 L48.

1107 Charbonneau, D., Brown, T. M., Noyes, R. W., Gilliland, R. L. 2002. Detec-  
1108 tion of an extrasolar planet atmosphere. *Astrophys. J.*, 568, 377–384.

1109 Charbonneau, D., et al., 2005. Detection of thermal emission from an extra-  
1110 solar planet. *Astrophys. J.*, 626, 523–529.

1111 Cooper, C. S., Sudarsky, D., Milsom, J. A., Lunine, J. I., Burrows, A., 2003.  
1112 Modeling the formation of clouds in brown dwarf atmospheres. *Astrophys.*  
1113 *J.*, 586, 1320–1337.

1114 Coustenis, A., et al., 1997. Spectroscopy of 51 Peg b: Search for atmospheric  
1115 signatures. *Planets beyond the solar system and the next generation of*  
1116 *space missions*, ASP Conf. Ser., 119, 101–105.

1117 Coustenis, A. et al., 1998. High resolution ground-based spectroscopy of 51

1118 Peg b: Search for atmospheric signatures. *Brown dwarfs and extrasolar*  
1119 *planets*, ASP Conf. Ser., 134, 296–303.

1120 Curdt, W., et al., 2001. The SUMER spectral atlas of solar-disk features.  
1121 *Astron. Astrophys.*, 375, 591–613.

1122 Curdt, W., Tian, H., Teriaca, L., Schuhle, U., Lemaire, P., 2008. The Ly- $\alpha$   
1123 profile and center-to-limb variations of the quiet Sun. *Astron. Astrophys.*,  
1124 492, L9–L12.

1125 Deming, D., Seager, S., Richardson, L. J., Harrington, J., 2005. Infrared  
1126 radiation from an extrasolar planet. *Nature*, 434, 740–743.

1127 Ekenbäck, A., et al., 2010. Energetic neutral atoms around HD209458b: Es-  
1128 timations of magnetospheric properties. *Astrophys. J.*, 709, 670–679.

1129 Flasar, F. M., et al., 2005. Temperatures, winds, and composition on the  
1130 Saturnian system. *Science*, 307, 1247–1251.

1131 Fletcher, L. N., Orton, G. S., Teanby, N. A., Irwin, P. G. J., Bjoraker, G.  
1132 L., 2009. Methane and its isotopologues on Saturn from Cassini/CIRS  
1133 observations. *Icarus*, 199, 351–367.

1134 Fortney, J. J., et al., 2003. On the indirect detection of sodium in the at-  
1135 mosphere of the planetary companion to HD209458b. *Astrophys. J.*, 589,  
1136 615–622.

1137 Fouchet, T., Moses, J. I., Conrath, B. J., 2009. Saturn: Composition and  
1138 chemistry. *Saturn from Cassini-Huygens* (p. 83–112). Springer, Dordrecht,  
1139 Germany.

1140 France, K., et al., 2010. Searching for far-ultraviolet auroral/dayglow emis-  
1141 sion from HD209458b. *Astrophys. J.*, 712, 1277–1286.

1142 Fossati, L., et al., 2010. Metals in the exosphere of the highly irradiated  
1143 planet WASP-12b. *Astrophys. J. Lett.*, 714, L222–L227.

1144 Garcia Munoz, A. 2007. Physical and chemical aeronomy of HD209458b.  
1145 *Plan. Sp. Sci.*, 55, 1426–1455.

1146 Gladstone, G. R., 1992. Solar O I 1304-Å triplet line profiles. *J. Geophys.*  
1147 *Res.*, 97, A12, 19519–19525.

1148 Griesmeier, J.-M., et al., 2004. The effect of tidal locking on the magneto-  
1149 spheric and atmospheric evolution of "Hot Jupiters". *Astron. Astrophys.*,  
1150 425, 753–762.

1151 Guillot, T., Gautier, D., 2007. Giant Planets, In: *Treatise on Geophysics,*  
1152 *Planets, and Moons*, vol. 10. Elsevier, Amsterdam, pp.439–464.

1153 Henry, G. W., Marcy, G. W., Butler, R. P., Vogt, S. S., 2000. A transiting  
1154 "51 Peg-like" planet. *Astrophys. J. Lett.*, 529, L41–L44.

1155 Holström, M., Ekenback, A., Selsis, F., Lammer, H., Wurz, P., 2008. Energetic

1156 neutral atoms as the explanation for the high-velocity hydrogen around  
1157 HD209458b. *Nature*, 451, 970–972.

1158 Holton, J. R., 2004. An introduction to dynamic meteorology. Elsevier Aca-  
1159 demic Press, London, England.

1160 Hummer, D. G., Seaton, M. J., 1963. The ionization structure of planetary  
1161 nebulae. *Mon. Not. R. Astron. Soc.*, 125, 437–459.

1162 Hunten, D. M., Pepin, R. O., Walker, J. C. G., 1987. Mass fractionation in  
1163 hydrodynamic escape. *Icarus*, 69, 532–549.

1164 Judge, P. G., Carlsson, M., Stein, R. F., 2003. On the origin of the basal  
1165 emission from stellar atmospheres: Analysis of solar C II lines. *Astrophys.*  
1166 *J.*, 597, 1158–1177.

1167 Knutson, H. A., Charbonneau, D., Noyes, R. W., Brown, T. M., Gilliland,  
1168 R. L., 2007. Using stellar limb-darkening to refine the properties of  
1169 HD209458b. *Astrophys. J.*, 655, 564–575.

1170 Knutson, H. A., Charbonneau, D., Allen, L. E., Burrows, A., Megeath, S.  
1171 T., 2008. The 3.6–8.0  $\mu\text{m}$  broadband emission spectrum of HD209458b:  
1172 Evidence for an atmospheric temperature inversion. *Astrophys. J.*, 673,  
1173 526–531.

1174 Koskinen, T. T., Yelle, R. V., Lavvas, P., Lewis, N., 2010a. Characterizing  
1175 the thermosphere of HD209458b with UV transit observations. *Astrophys.*  
1176 *J.*, 723, 116–128.

1177 Koskinen, T. T., Harris, M., Yelle, R. V., Lavvas, P., 2012. The escape  
1178 of heavy atoms from the ionosphere of HD209458b. I. A photochemical-  
1179 dynamical model of the thermosphere. *Icarus*, *submitted*

1180 Lammer, H., Kislyakova, K. G., Holstrom, M., Khodachenko, M. L., Gries-  
1181 meier, J.-M., 2011. Hydrogen ENA-cloud observation and modeling as a  
1182 tool to study star-exoplanet interaction. *Astrophys. Space Sci.*, 335, 9–23.

1183 Lites, B. W., Shine, R. A., Chipman, E. G., 1978. Line formation in the solar  
1184 chromosphere. I. The C II resonance lines observed with OSO 8. *Astrophys.*  
1185 *J.*, 222, 333–341.

1186 Lecavelier des Etangs, A., et al., 2010. Evaporation of the planet HD189733b  
1187 observed in H I Lyman  $\alpha$ . *Astron. Astrophys.*, 514, A72.

1188 Lemaire, P., et al., 2005. Variation of the full Sun hydrogen Lyman profiles  
1189 through solar cycle 23. *Adv. Space Sci.*, 35, 384–387.

1190 Linsky, J. L., et al. 2010. Observations of mass loss from the transiting exo-  
1191 planet HD209458b. *Astrophys. J.*, 717, 1291–1299.

1192 Lodders, K., 2003. Solar system abundances and condensation temperatures  
1193 of the elements. *Astrophys. J.*, 591, 1220–1247.

1194 Mahaffy, P. R., et al., 2000. Noble gas abundance and isotope ratios in the  
1195 atmosphere of Jupiter from the Galileo Probe Mass Spectrometer. *J. Geo-*  
1196 *phys. Res.*, 105, E6, 15,061–15,071.



1197 Morton, D. C., 1991. Atomic data for resonance absorption lines. I. Wave-  
1198 lengths longward of the Lyman limit. *Astrophys. J. Supp.*, 77, 119–202.

1199 Morton, D. C., 2003. Atomic data for resonance absorption lines. III. Wave-  
1200 lengths longward of the Lyman limit for the elements hydrogen to gallium.  
1201 *Astrophys. J. Supp*, 149, 205–238.

1202 Moses, J. I., et al., 2011. Disequilibrium carbon, oxygen, and nitrogen chem-  
1203 istry in the atmospheres of HD189733b and HD209458b. *Astrophys. J.*,  
1204 737, 15.

1205 Moutou, C., et al., 2001. Search for spectroscopical signatures of transiting  
1206 HD209458b exosphere. *Astron. Astrophys.*, 371, 260–266.

1207 Moutou, C., Coustenis, A., Schneider, J., Queloz, D., Mayor, M., 2003.  
1208 Searching for helium in the exosphere of HD209458b. *Astron. Astrophys.*,  
1209 405, 341–348.

1210 Murray-Clay, R. A., Chiang, E. I., Murray, N., 2009. Atmospheric escape  
1211 from Hot Jupiters. *Astrophys. J.*, 693, 23–42.

1212 Narita, N., et al., 2005. Subaru HDS transmission spectroscopy of the transit-  
1213 ing extrasolar planet HD209458b. *Publ. Astron. Soc. Japan*, 57, 471–480.

1214 Nicolas, K. R., et al., 1977. Solar EUV emission line profiles of Si II and Si  
1215 III and their center to limb variations. *Sol. Phys.*, 55, 305–319.

1216 Nicolas, K. R., Kjeldseth-Moe, O., Bartoe, J.-D. F., Brueckner, G. E., 1982.  
1217 High resolution EUV structure of the chromosphere-corona transition re-  
1218 gion above a sunspot. *Sol. Phys.*, 81, 253–280.

1219 Owen, T., Encrenaz, T., 2003. Element abundances and isotope ratios in the  
1220 giant planets and Titan. *Space Sci. Rev.*, 106, 121–138.

1221 Parker, E. N., 1964a. Dynamical properties of stellar coronas and stellar  
1222 winds. I. Integration of the momentum equation. *Astrophys. J.*, 139, 72–  
1223 92.

1224 Richardson, L. J., Deming, D., Horning, K., Seager, S., Harrington, J., 2007.  
1225 A spectrum of an extrasolar planet. *Nature*, 445, 892–895.

1226 Roussel-Dupre, D., 1985. SKYLAB observations of the solar O I resonance  
1227 triplet. *Astron. Astrophys.*, 153, 116–124.

1228 Schunk, R. W., Nagy, A. F., 2000. Ionospheres: Physics, plasma physics, and  
1229 chemistry. Cambridge University Press, Cambridge, England.

1230 Schlawin, E., Agol, E., Walkowicz, L. M., Covey, K., Lloyd, J. P., 2010.  
1231 Exoplanetary transits of limb-brightened lines: Tentative Si IV absorption  
1232 by HD209458b. *Astrophys. J. Lett.*, 722, L75–L79.

1233 Schneider, J., Rauer, H., Lasota, J. P., Bonazzola, S., Chassefiere, E., 1998.  
1234 The cometary tail of giant extrasolar planets at small orbital distances.  
1235 *Brown dwarfs and extrasolar planets*, ASP Conf. Ser., 134, 241–244.

1236 Seager, S., Sasselov, D. D., 2000. Theoretical transmission spectra during  
1237 extrasolar giant planet transits. *Astrophys. J.*, 537, 916–921.

1238 Sing, D. K., Vidal-Madjar, A., Desert, J.-M., Lecavelier des Etangs, A.,  
1239 Ballester, G., 2008a. Hubble Space Telescope STIS optical transit trans-  
1240 mission spectra of the hot Jupiter HD209458b. *Astrophys. J.*, 686, 658–666.

1241 Sing, D. K., et al., 2008b. Determining atmospheric conditions at the termi-  
1242 nator of the hot Jupiter HD209458b. *Astrophys. J.*, 686, 667–673.

1243 Showman, A., et al., 2009. Atmospheric circulation of hot Jupiters: Coupled  
1244 radiative-dynamical general circulation model simulations of HD189733b  
1245 and HD209458b. *Astrophys. J.*, 699, 564–584.

1246 Silva-Valio, A., 2008. Estimating stellar rotation from starspot detection dur-  
1247 ing planetary transits. *Astrophys. J.*, 683, L179–L182.

1248 Spiegel, D. S., Silverio, K., Burrows, A., 2009. Can TiO explain thermal  
1249 inversions in the upper atmospheres of irradiated giant planets. *Astrophys.*  
1250 *J.*, 699, 1487–1500.

1251 Swain, M. R., Bouwman, J., Akeson, R. L., Lawler, S., Beichman, C. A.,  
1252 2008. The mid-infrared spectrum of the transiting exoplanet HD209458b.  
1253 *Astrophys. J.*, 674, 482–497.

1254 Swain, M. R., et al., 2009. Water, methane, and carbon dioxide present in  
1255 the dayside spectrum of the exoplanet HD209458b. *Astrophys. J.*, 704,  
1256 1616–1621.

1257 Tian, F., Toon, O. B., Pavlov, A. A., de Sterck, H., 2005. Transonic hy-  
1258 drodynamic escape of hydrogen from extrasolar planetary atmospheres.  
1259 *Astrophys. J.*, 621, 1049–1060.

1260 Trammell, G. B., Arras, P., Li, Z.-Y., 2011. Hot Jupiter magnetospheres.  
1261 *Astrophys. J.*, 728, 152.

1262 Tobiska, W. K., et al., 2000. The SOLAR2000 empirical solar irradiance  
1263 model and forecast tool. *J. Atmos. Sol.-Terr. Phys.*, 62, 1233–1250.

1264 Vidal-Madjar, A., et al., 2003. An extended upper atmosphere around the  
1265 extrasolar giant planet HD209458b. *Nature*, 422, 143–146.

1266 Vidal-Madjar, A., et al., 2004. Detection of oxygen and carbon in the hy-  
1267 drodynamically escaping atmosphere of the extrasolar planet HD209458b.  
1268 *Astrophys. J. Lett.*, 604, L69–L72.

1269 Vidal-Madjar, A., et al., 2011a. The upper atmosphere of the exoplanet  
1270 HD209458b revealed by the sodium D lines: Temperature–pressure pro-  
1271 file, ionization layer, thermosphere. *Astron. Astrophys.*, 527, A110.

1272 Vidal-Madjar, A., et al., 2011b. The upper atmosphere of the exoplanet  
1273 HD209458b revealed by the sodium D lines: Temperature–pressure profile,  
1274 ionization layer, thermosphere (Corrigendum). *Astron. Astrophys.*, 533,  
1275 C4.

1276 Visscher, C., Lodders, K., Fegley, B., Jr., 2010. Atmospheric chemistry in gi-

1277 ant planets, brown dwarfs, and low-mass dwarf stars. III. Iron, magnesium,  
1278 and silicon. *Astrophys. J.*, 716, 1060–1075.

1279 Winn, J., et al., 2004. A search for H $\alpha$  absorption in the exosphere of the  
1280 transiting extrasolar planet HD209458b. *Publ. Astron. Soc. Japan*, 56,  
1281 655–662.

1282 Wong, M. H., Mahaffy, P. R., Atreya, S. K., Niemann, H. B., Owen, T. C.,  
1283 2004. Updated Galileo probe mass spectrometer measurements of carbon,  
1284 oxygen, nitrogen, and sulfur on Jupiter. *Icarus*, 171, 153–170.

1285 Wood, B. E., Linsky, J. L., 1997. A new measurement of the electron density  
1286 in the local interstellar medium. *Astrophys. J. Lett.*, 474, L39–L42.

1287 Wood, B. E., Redfield, S., Linsky, J. L., Muller, H.-R., Zank, G. P., 2005.  
1288 Stellar Ly $\alpha$  emission lines in the Hubble Space Telescope archive: Intrinsic  
1289 line fluxes and absorption from the heliosphere and astropheres. *Astrophys.*  
1290 *J. Supp.*, 159, 118–140.

1291 Woods, T. N., Tobiska, W. K., Rottman, G. J., Worden, J. R., 2000. Im-  
1292 proved solar Lyman  $\alpha$  irradiance modeling from 1947 through 1999 based  
1293 on UARS observations. *J. Geophys. Res.*, 105, A12, 27195–27215.

1294 Woods, T. N., Rottman, G. J., 2002. Solar ultraviolet variability over time pe-  
1295 riods of aeronomical interest. In: Mendillo, M., et al. (Eds.), *Comparative*  
1296 *aeronomy in the solar system*. American Geophysical Union Monograph.

- 1297 Worden, J. R., White, O. R., Woods, T. N., 1998. Evolution of chromospheric  
1298 structures derived from Ca II K spectroheliograms: Implications for solar  
1299 ultraviolet irradiance variability. *Astrophys. J.*, 496, 998–1014.
- 1300 Yelle, R. V., 2004. Aeronomy of extra-solar giant planets at small orbital  
1301 distances. *Icarus*, 170, 167–179.
- 1302 Zahnle, K. J., Kasting, J. F., 1986. Mass fractionation during transonic es-  
1303 cape and its implications for loss of water from Mars and Venus. *Icarus*,  
1304 68, 462–480.
- 1305 Zhanle, K., Marley, M. S., Freedman, R. S., Lodders, K., Fortney, J. J., 2009.  
1306 Atmospheric sulfur photochemistry on hot Jupiters. *Astrophys. J. Lett.*,  
1307 701, L20–L24.